NUREG/CR-3023
SAND82-2475
R7
Printed March 1984

# Molten Thermite Teeming Into an Iron Oxide Particle Bed

W. W. Tarbell, R. E. Blose, F. E. Arellano

Prepared by
Sandia National Laboratories
Albuquerque, New Mexico 87185 and Livermore, California 94550
for the United States Department of Energy
under Contract DE-AC04-76DP00789

**Prepared for**
**U. S. NUCLEAR REGULATORY COMMISSION**

SF 2900-Q(6-82)
8405220033 840430
PDR NUREG
CR-3023 R PDR

**NOTICE**

This report was prepared as an account of work sponsored by an agency of the United States Government. Neither the United States Government nor any agency thereof, or any of their employees, makes any warranty, expressed or implied, or assumes any legal liability or responsibility for any third party's use, or the results of such use, of any information, apparatus product or process disclosed in this report, or represents that its use by such third party would not infringe privately owned rights.

Available from

GPO Sales Program
Division of Technical Information and Document Control
U.S. Nuclear Regulatory Commission
Washington, D.C. 20555

and

National Technical Information Service
Springfield, Virginia 22161

NUREG/CR-3023
SAND82-2475
R7

# MOLTEN THERMITE TEEMING INTO AN IRON OXIDE PARTICLE BED

W. W. Tarbell*
R. E. Blose*
F. E. Arellano

March 1984

Sandia National Laboratories
Albuquerque, NM 87185
Operated by
Sandia Corporation
for the
U.S. Department of Energy

Prepared for
Division of Reactor Safety Research
Office of Nuclear Regulatory Research
U.S. Nuclear Regulatory Commission
Washington, D.C. 20555
Under Memorandum of Understanding DOE 40-550-75
NRC FIN No. A-1247

*Ktech Corporation

## ABSTRACT

The two particle bed tests employed 10-kg thermite melts (2700°K) teemed into a bed of iron oxide particles. The objective of the experiments was to investigate bed penetration, particle floatation and fracture, and heat flux partitioning. The results show that the hydraulic forces exerted by the melt did not immediately displace the bed. Bed penetration was by melting and absorbing of the particles with the major portion of the displaced iron oxide terminating in the alumina phase of the melt. The movement of the penetration front suggests the movement to be a series of melt/freeze/remelt processes. The large grain structure of the iron phase indicates that the cooling was slow and continuous. A coherent 1-cm-thick layer of iron oxide in contact with the melt was created by sintering of the particles. The particle size of the unaffected portions of the bed showed very little fracturing due to thermal stress and slightly over 7% particle growth due to sintering. The calculated heat flux values to the surrounding crucible structure suggest that the bed is effective in delaying and reducing the magnitude of the peak heat flux values.

TABLE OF CONTENTS


| | | Page |
|---|---|---|
| I. | Introduction | 1 |
| II. | Test Apparatus | 3 |
| III. | Experimental Observations | 11 |
| | A. Test Sequence | 11 |
| | B. Test Observations | 11 |
| | C. Posttest Examination | 17 |
| IV. | Results and Discussion | 24 |
| | A. Metallography of Iron Phase | 24 |
| | B. Metallography of Iron Oxide Layer | 26 |
| | C. Metallography of Alumina Phase | 32 |
| | D. Iron Oxide Particle Size | 35 |
| | E. Heat Flux Results | 37 |
| | F. Thermal Conductivity Correlations | 41 |
| V. | Summary | 43 |
| APPENDIX A -- Thermocouple Temperature Histories | | 45 |
| APPENDIX B -- Heat Flux Calculations | | 53 |
| REFERENCES | | 62 |

LIST OF ILLUSTRATIONS


| Figure | | Page |
|---|---|---|
| 1. | Test Setup for PARTICLE BED I and II Experiments. . . . . | 4 |
| 2. | Thermocouple Locations in PARTICLE BED II Experiment . . . . . | 6 |
| 3. | Crucible Thermocouple Locations for PARTICLE BED II Experiment. . . . . | 6 |
| 4. | Typical Crucible Thermocouple Installations for PARTICLE BED II Experiment . . . . . | 7 |
| 5. | Iron Oxide Particle Shapes . . . . . | 9 |
| 6. | Geometric Description of Iron Oxide PARTICLE BED II . . . . . | 9 |
| 7. | Photograph of Image-Enhanced Video X-Ray Record (Time = 1.0 Sec) . . . . . | 12 |
| 8. | Photograph of Image-Enhanced Video X-Ray Record (Time = 8.5 Sec) . . . . . | 12 |
| 9. | Photograph of Image-Enhanced Video X-Ray Record (Time = 13.0 Sec). . . . . | 13 |
| 10. | Photograph of Image-Enhanced Video X-Ray Record (Time = 13.3 Sec). . . . . | 13 |
| 11. | Photograph of Image-Enhanced Video X-Ray Record (Time = 15.0 Sec). . . . . | 14 |
| 12. | Photograph of Image-Enhanced Video X-Ray Record (Time = 30.0 Sec). . . . . | 14 |
| 13. | Photograph of Image-Enhanced Video X-Ray Record (Time = 40.0 Sec). . . . . | 15 |
| 14. | Photograph of Image-Enhanced Video X-Ray Record (Time = 50.0 Sec). . . . . | 15 |
| 15. | Melt Penetration into Iron Oxide Particle Bed. . . | 18 |
| 16a. | Posttest Front Profile for PARTICLE BED II Experiment . . . . . | 19 |
| 16b. | Posttest Cross-Sectional Side Profile for PARTICLE BED II Experiment . . . . . | 19 |

LIST OF ILLUSTRATION (Cont'd)


| Figure | | Page |
|---|---|---|
| 17. | Photograph of Sectioned Alumina and Iron Phase . . | 21 |
| 18a. | Photograph of Sectioned Iron Phase Showing Interior Structure . . . . . | 22 |
| 18b. | Photograph of Sectioned Iron Phase Showing Outer Surface. . . . . | 22 |
| 19. | Photomicrograph of Polished and Etched Quarter-Section of the Metallic Phase from PARTICLE BED II . . . . . | 25 |
| 20. | Photomicrograph (25X Magnification) of Region Near the Periphery of the Iron Phase . . . . . | 25 |
| 21. | Photomicrograph (25X Magnification) of Region Near the Center of the Iron Phase. . . . . | 25 |
| 22. | Cross-Sectional Photomicrograph of Coherent Iron Oxide Layer Found Between the Iron Phase (Above) and Undisturbed Iron Oxide Particle Bed (Below). . . . . | 27 |
| 23. | Photomicrograph of Coherent Iron Oxide Region Closest to the Iron Phase. . . . . | 28 |
| 24. | X-Ray Analysis of Coherent Iron Oxide Layer Closest to the Iron Phase. . . . . | 30 |
| 25. | Photomicrographs of Coherent Iron Oxide Layer Showing Transition Region. . . . . | 31 |
| 26. | Photomicrograph of Coherent Iron Oxide Layer Showing Region of Sintered Particles . . . . . | 32 |
| 27. | Photomicrograph at 100X Magnification of a Portion of Alumina Phase . . . . . | 33 |
| 28. | Electron Microprobe Analysis of Alumina Phase Region. (A) - Aluminum (Al); (B) - Iron (Fe); (C) - Silica (Si). . . . . | 35 |
| 29. | Photomicrograph at 400X Magnification of Interstitial Area of Alumina Phase . . . . . | 36 |
| 30. | Electron Microprobe Analyses of Interstitial Area. (A) - Aluminum (Al); (B) - Iron (Fe); (C) - Silica (Si). . . . . | 36 |

LIST OF ILLUSTRATIONS (Cont'd)


| Figure | | Page |
|---|---|---|
| 31. | Temperature Histories for Top and Upper Middle Crucible Sidewall Thermocouples. . . . . | 39 |
| 32. | Total Heat Calculations at the Surface Adjacent to Thermocouple Locations. . . . . | 40 |
| 33. | Correlation of Peak Heat Flux vs. Thickness of PARTICLE BED at Measurement Location. . . . . | 41 |
| A-1. | Brick TC Data PARTICLE BED II -- Brick Back Plane Bottom . . . . . | 47 |
| A-2. | Brick TC Data PARTICLE BED II -- Brick Right Side Top . . . . . | 47 |
| A-3. | Brick TC Data PARTICLE BED II -- Brick Left Side Bottom. . . . . | 48 |
| A-4. | Crucible TC Data PARTICLE BED II -- Top Side Plane. . . . . | 48 |
| A-5. | Crucible TC Data PARTICLE BED II -- Upper Middle Side Plane . . . . . | 49 |
| A-6. | Crucible TC Data PARTICLE BED II -- Lower Middle Side Plane . . . . . | 49 |
| A-7. | Crucible TC Data PARTICLE BED II -- Bottom Side Plane. . . . . | 50 |
| A-8. | Crucible TC Data PARTICLE BED II -- Half-Radius Side Plane . . . . . | 50 |
| A-9. | Crucible TC Data PARTICLE BED II -- Top Rear Plane. . . . . | 51 |
| A-10. | Crucible TC Data PARTICLE BED II -- Upper Middle Rear Plane . . . . . | 51 |
| A-11. | Crucible TC Data PARTICLE BED II -- Lower Middle Rear Plane . . . . . | 52 |
| A-12. | Crucible TC Data PARTICLE BED II -- Bottom Rear Plane. . . . . | 52 |
| A-13. | Crucible TC Data PARTICLE BED II -- Half-Radius Rear Plane . . . . . | 53 |
| A-14. | Crucible TC Data PARTICLE BED II -- Center Bottom . . . . . | 53 |

LIST OF TABLES


| Table | | Page |
|---|---|---|
| I. | Events in the PARTICLE BED II Experimental Sequence | 16 |
| II. | Mass of Alumina and Iron Phases. | 20 |
| III. | Mass of Displaced Iron Oxide | 23 |
| IV. | Posttest Sieve Analysis of Iron Oxide Particle Bed. | 37 |
| B-1. | Values and Time of Maximum Heat Flux | 57 |
| B-2. | Parametric Values Obtained for Qualification of the Estimation Procedure. | 61 |

# I. Introduction

In the unlikely event of a severe nuclear reactor accident, the core may overheat, melt, and attack the pressure vessel. If the vessel fails, the interactions of the molten core debris with structural containment materials become the dominant contributors to the eventual outcome of the event. It has been shown that molten debris can vigorously attack reactor concretes causing large quantities of aerosols and noncondensable gases to be released (Refs 1, 2). As these materials enter the containment atmosphere, significant loadings are placed on the engineered safety features and threaten the integrity of the containment structure. The aerosol may also carry fission products that can be a health hazard, particularly if the containment building fails.

Much interest has been shown in the use of retrofit safety features that reduce or eliminate the ex-vessel core/concrete interactions. One candidate solution is to cover the floor and sides of the cavity beneath the reactor pressure vessel with a bed of particle material. The particle bed prevents the immediate contact of the concrete by the core debris and provides a large heat sink to absorb some of the decay-heat energy of the debris. Particle beds (also known as gravel or rubble beds) are particularly attractive because of their potentially low cost of installation in existing plants. This cost advantage may be offset, however, if highly exotic materials are required for the bed material. A more extensive treatment of the particle-bed core retention concept is given in Reference 3.

The test program described in this report was designed to address the following questions regarding particle-bed retention devices:

(1) Will hydraulic forces exerted by the melt stream cause immediate displacement of the bed?

(2) Does the density of the bed need to be greater than the density of the core debris to prevent penetration by particle flotation?

(3) Must a refractory, high-melting-temperature bed material be used to prevent particle thermal shock or melting?

(4) How does the bed affect heat flux to the structures surrounding the bed?

Two tests were performed using a thermitically generated iron/alumina melt that was drained teeming onto a bed of iron-oxide particles. The thermite reaction is a convenient method of creating a high-temperature (nominally 2700°K) mixture of metal

and metallic oxide to simulate degraded core debris. Iron oxide is less dense than the metallic phase of the melt and is not considered highly refractory or thermal-shock resistant. Thus, the bed provides an opportunity to evaluate the extent of particle floating and fracturing.

Real-time X-ray imaging was used on the tests to monitor melt penetration into the particle bed. This technique allows nonintrusive observation of the in-depth interaction, providing valuable information that cannot be found by other means. Thermocouple sensors are also used to infer the heat flux partitioning from the melt to the crucible representing the position of the concrete basemat and sidewalls.

Two identical tests were performed as part of this study (PARTICLE BED I and II). The thermocouple and X-ray video data from the first test were of poor quality, necessitating the second test. This report deals primarily with the results from the second of the two tests.

## II. Test Apparatus

The test apparatus is designed to generate the melt separately and then introduce it onto the particle bed in a controlled fashion. Figure 1 is a schematic representation of the device. The top section consists of a melt generator that contains the thermite mixture and the bottom section that holds the iron oxide particle bed.

The melt generator is constructed of a 100-lb-capacity (in steel), thin-wall, fused-alumina crucible* of "classical" shape. A 12-mm-diameter hole is drilled in the bottom of the crucible to accept a fusible copper plug. The plug retains the mixture until the reaction front causes failure and the molten mixture drains through the hole. The crucible is capped by a series of steel plates and short pipe sections to form two expansion chambers that filter and vent the thermite reaction gases. Sealing between the individual components is accomplished using several layers of graphite foil.** Each plate is drilled with 6 holes (12.5-mm diameter) to allow gas to escape. The stainless steel turnings in the upper chamber are designed to prevent escape of melt particles carried by the gas stream.

The thermite melt is generated using the exothermic chemical reaction

$$3Fe_3O_4 + 8Al \longrightarrow 9Fe + 4Al_2O_3 + \text{heat}$$

with a heat of reaction estimated to be approximately $3.6 \times 10^6$ Joule/kg. For the ten kilograms used, 7629 grams of magnetite*** ($Fe_3O_4$) and 2371 grams of aluminum+ are required. The reaction is initiated by passing an electrical current through a section of embedded Pyrofuse.++ The maximum theoretical temperature (no

---

*A product of Norton Company Industrial Ceramics Division, Worchester, Mass., 01606.

**Graphfoil, Union Carbide Corporation, Chicago, Ill., 60606.

***Grade MS-30 (74 to 600- m particle size), Chemalloy Company, Inc., Bryn Mawr, PA, 19010.

+Less than 140- m particle size, obtained from Alcoa Conductive Products Division, Oklahoma City, OK.

++Pyrofuse Corporation, an affiliate of Sigmund Cohn Corporation, Mt. Vernon, NY.

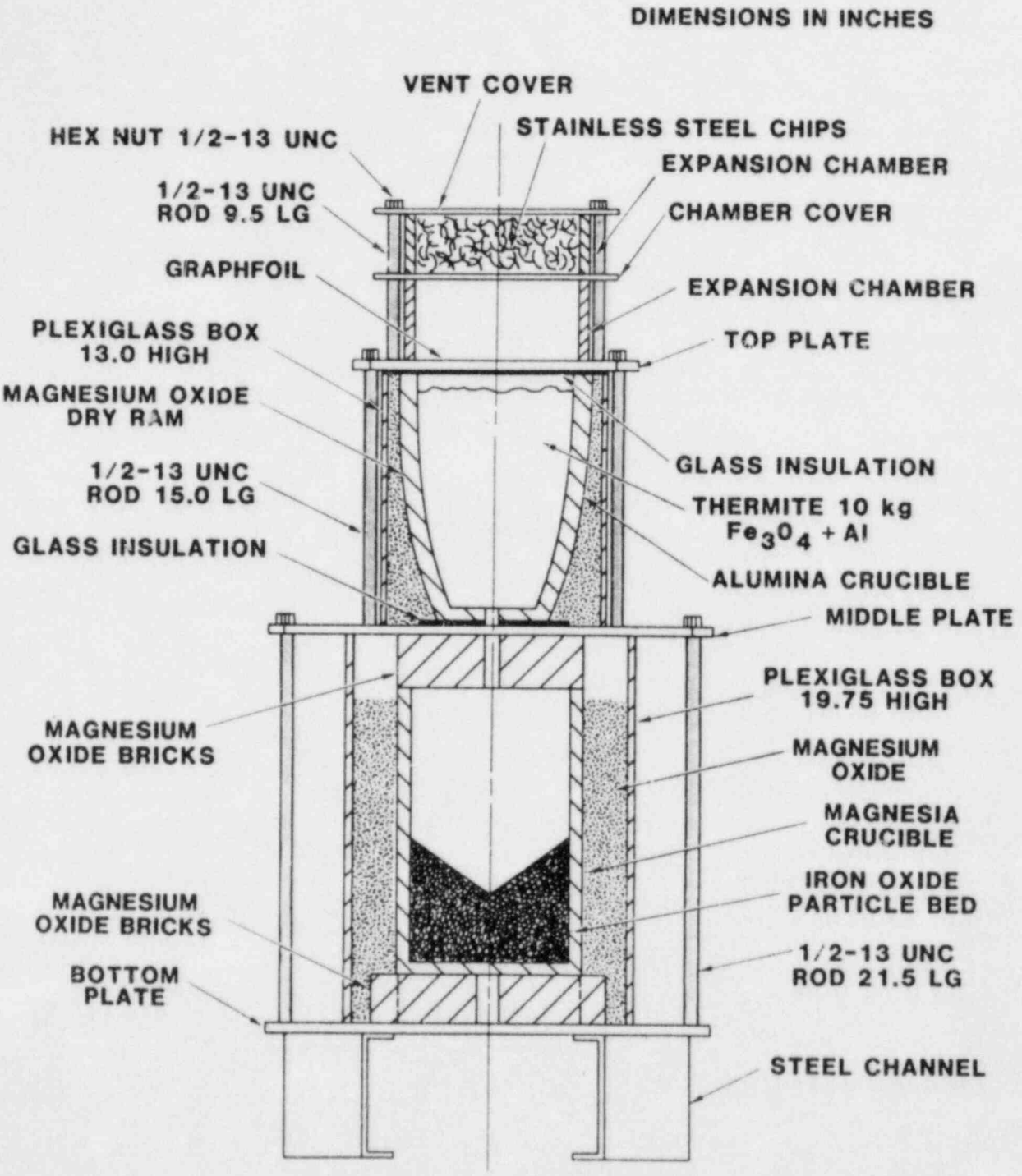


Figure 1. Test Setup for PARTICLE BED I and II Experiments

heat losses) if the reaction goes to completion is estimated to be 3000 K (Ref 4); however melt temperature measurements were not attempted. The actual temperature is estimated to be on the order of 2700 K for these experiments.

The melt generator section is separated from the lower section by three magnesium oxide bricks* used to cap the crucible containing the particle bed. The center brick is instrumented with embedded thermocouples to monitor the temperature increase caused by radiation from the melt pool. These data are intended to infer the upward heat flux. Figure 2 shows details of the brick. The central 1.9-cm-diameter hole allows the thermite to pass from the melt generator to the bottom section of the apparatus. Chromel-alumel (Type K) thermocouples with stainless steel sheaths (1.58-mm diameter) are placed in each of the three drilled holes and held in place with a synthetic ceramic cement.** The distance of the sensing tip from the brick surface exposed to the melt is nominally 1.0 cm for each of the thermocouples. Two sensors are oriented with their sheaths parallel to the incident heat flux surface with the third sensor placed vertically. The two orientations were employed to assess the effect of heat conduction along the sheath away from the sensing tip.

The particle bed is formed within a standard (straight-wall) 150-lb capacity (in steel) magnesium oxide crucible.*** Nominal dimensions of the crucible are 22.9-cm OD x 19.8-cm ID x 36.8 cm in height. Thermocouples placed in the crucible sidewall and base measure the temperature induced by the heat transfer through the particle bed from the melt. The crucible rests on two magnesium oxide bricks spaced 5.1-cm apart to allow routing of the thermocouple leads away from the crucible. Figure 3 shows the locations of the thermocouples. Each thermocouple is mounted by drilling a 6.4-mm hole into the crucible to allow a portion of the thermocouple sheath to be oriented parallel to the incident heat flux surface (Figure 4). This procedure was selected to minimize the error induced by heat conduction along the sheath away from the sensing location. Sauereisen cement is used to hold the thermocouple in place. All crucible thermocouples are Chromel-alumel (Type K) in 1.6-mm-diameter stainless-steel sheaths.

---

*Harklase basic brick, Harbison-Walker Refractories, Division of Dresser Industries, Inc., Pittsburgh, PA, 15222.

**Sauereisen Cement #31, Sauereisen Cements Company, Pittsburgh, PA, 15238.

***Norton Industrial Ceramics Division, Worcester, MS, 01606.

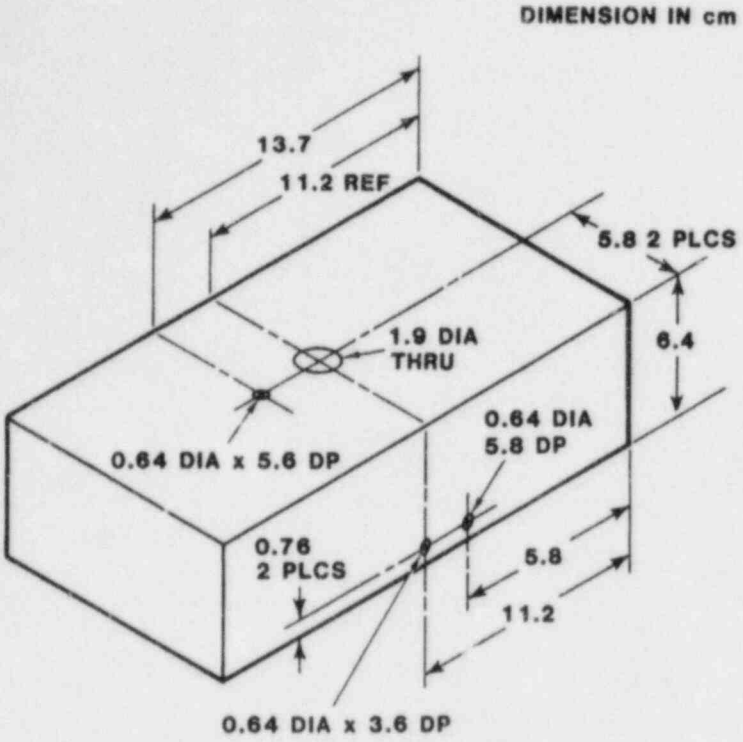


Figure 2.

Thermocouple Locations in PARTICLE BED II Experiment

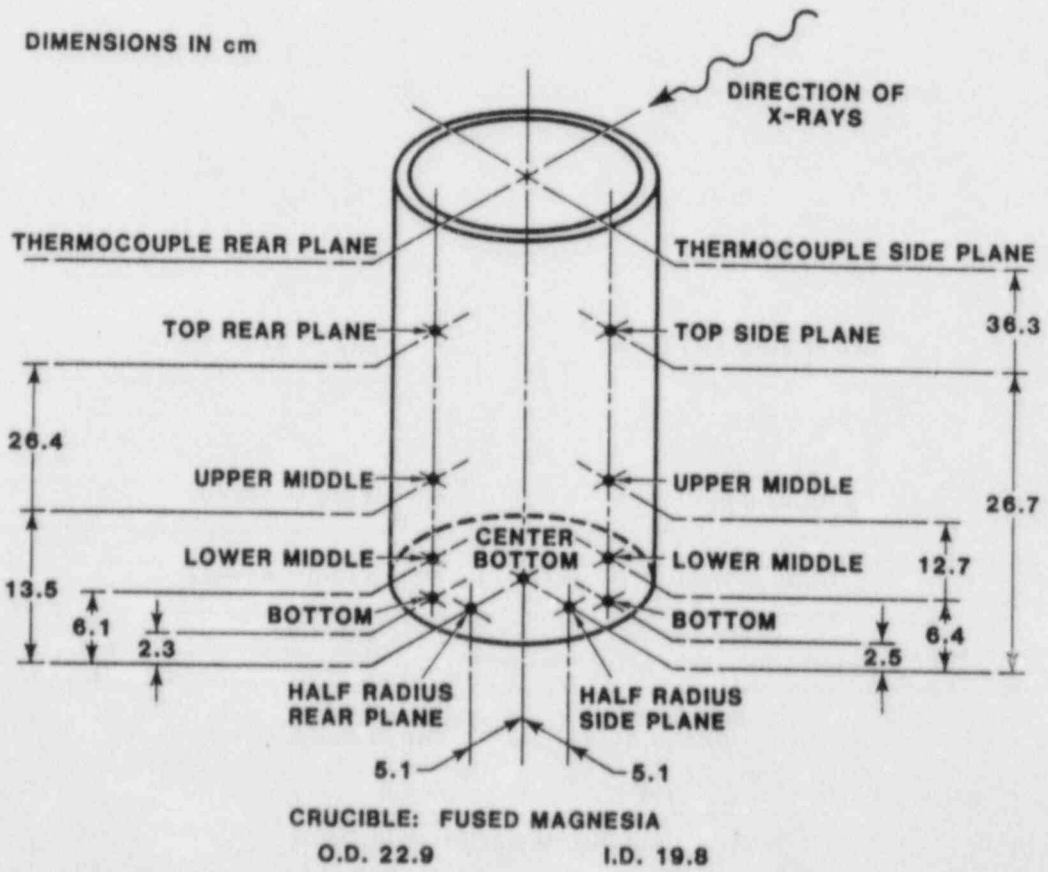


Figure 3. Crucible Thermocouple Locations for PARTICLE BED II Experiment

DIMENSIONS IN cm

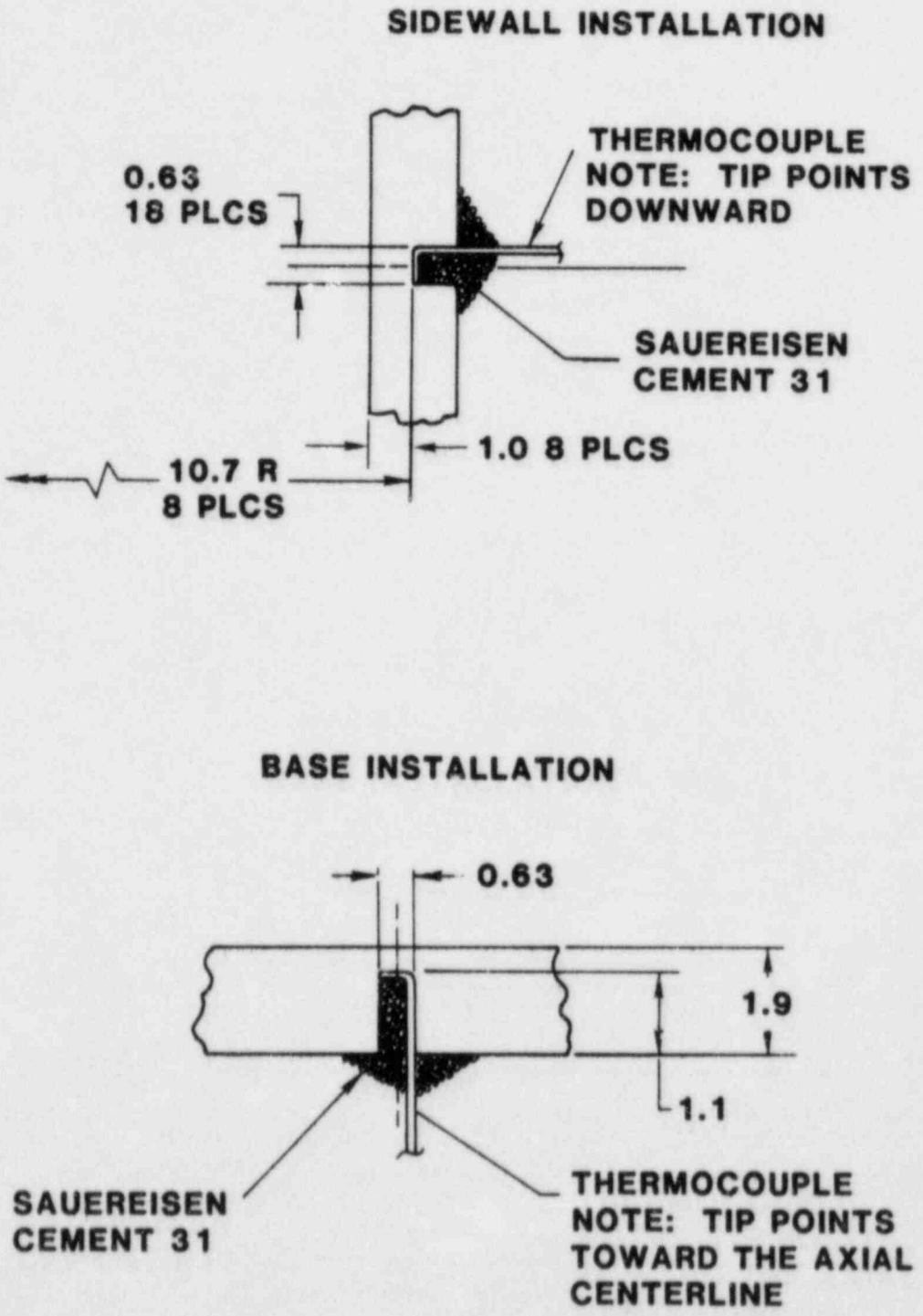


Figure 4. Typical Crucible Thermocouple Installations for PARTICLE BED II Experiment

The crucible and magnesium oxide bricks are held in place between the mild steel middle and bottom plates (see Figure 1). A square plexiglass box is used to retain the magnesium oxide dry-ramming material. The dry ram is intended to prevent the escape of hot material if the crucible fractures during the test. Plexiglass is used to minimize the attenuation of the X-rays.

Analysis of the particle-bed core retention gravel bed concept suggests that a possible mode of damage will be by mechanical removal of bed particles. Scaling of the mechanisms involved indicates that melt penetration or bed removal is related to the ratio of the stream diameters involved and the sizes of the particles employed. The size of the breach (i.e., stream size) in the reactor vessel can vary over a wide range. However, Large Break LOCA sequences (no system pressure) assume vessel failure to be extensive, up to the diameter of the reactor pressure vessel. The tests described here are best representative of a large-break LOCA sequence, i.e., an ambient pressure, gravity-accelerated stream. Particle size for candidate bed retention concepts has not been established, but a 3.8-cm diameter represents an average of the postulated range of sizes. Combining this dimension with an assumed stream size equivalent to the radius of a reactor pressure vessel yields an average test particle size of 281 m.

The particle size range selected for the tests give an average dimension corresponding to the scaled size of 281 m. The particles were obtained by mechanically sieving the same iron oxide material (magnetite) as used in preparing the thermite mixture. Two sieve sizes are used: 355 ± 16 m and 212 ± 10 m to obtain particles over this range. Figure 5 is a photo taken at 25X magnification of a portion of the particles obtained using the sieve sizes mentioned above. Inspection of the particles reveals them to be a mixture of angular and nearly spherical shapes.

The geometry of the particle bed is the intersection of two planar surfaces enscribed within the cylindrical crucible (Figure 6). The plane surfaces are angled from the horizontal at roughly the angle of repose for the material. The intent of using this geometry is to study the portion of a candidate bed where relocation is most likely to occur, i.e., the material "banked" against the cavity sidewalls. It is assumed that if particles are not removed in this geometry, the relatively flat portions of the bed will also not be affected.

The shape is formed by pouring the iron oxide particles into the crucible to form a base nominally 8.3-cm thick. After light tamping, the bulk density of the base material is calculated to be 3.04 g/cm$^3$, or roughly 42% porosity, based on theoretical density of solid magnetite (5.18 g/cm$^3$). The angled surfaces are formed by pouring the iron oxide particles into the crucible to obtain the maximum angle of repose. It was necessary to use a

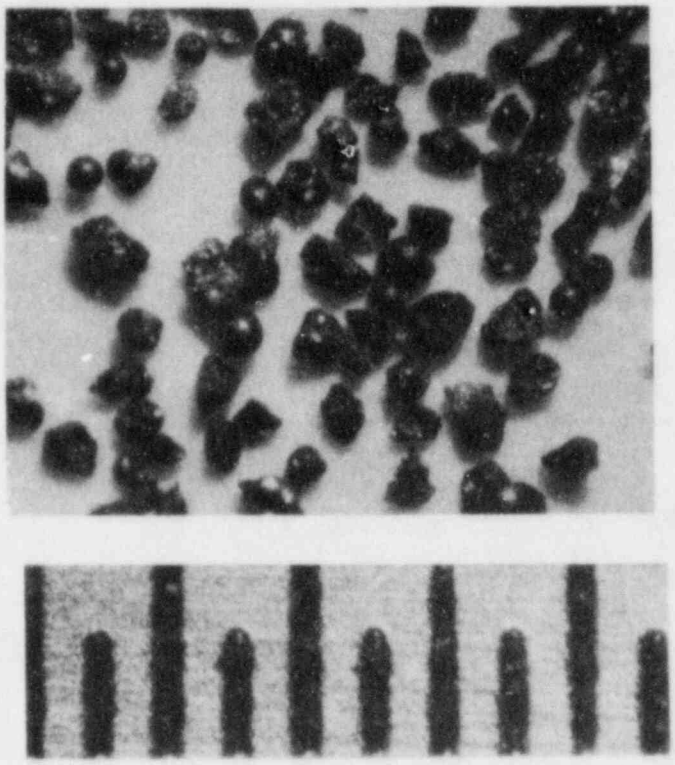

Figure 5. Iron Oxide Particle Shapes (Length scale is 0.5 mm per division)

ALL DIMENSIONS IN cm

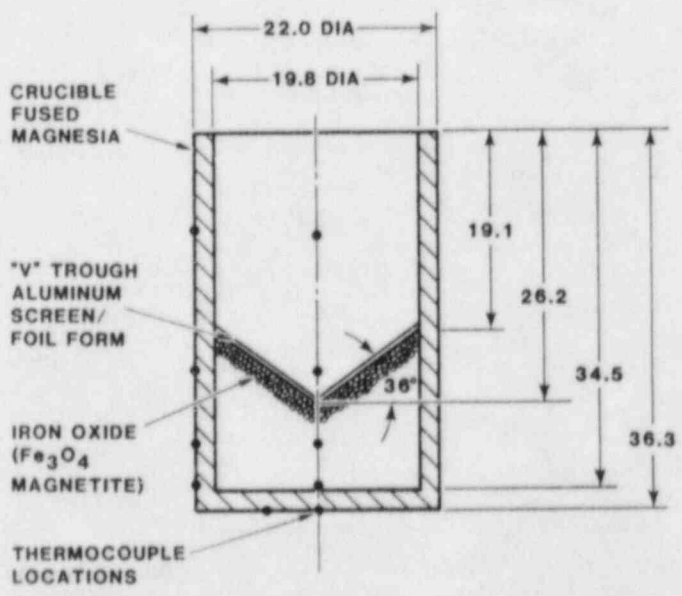


Figure 6. Geometric Description of Iron Oxide PARTICLE BED II (The line of intersection of the two plane surfaces is normal to the paper)

form of aluminum screen wire and a single-thickness of common household aluminum foil to aid in this procedure. The heat capacity of the form is very small and it is assumed to ablate upon contact with the melt. The angle obtained in this manner between the planar surfaces and horizontal is 35.8 degrees.

The interaction of the melt and particle bed was monitored by X-rays transmitted through the apparatus. The X-ray unit is a Linatron* model 1500 pulsed source with an X-ray voltage of 7.5 MeV and a dose rate of approximately 1000 rads/min. The source was placed 3.8 meters from the centerline of the test apparatus. Image collection was performed by a Decalix-SI** image intensification system with a 32-cm-diameter fluorescent screen aligned normal to the X-rays emerging from the apparatus. The device converts the photons from the fluorescent screen into electrons that are then focused onto a television camera.

The television image consists of 525 lines interlaced at 30 frames per second with a maximum resolution of 9 line pairs per centimeter. The sharpness of the X-ray image (absence of edge blurring) cannot be better than approximately 0.5 mm, principally because of geometric unsharpness caused by nonparallel rays. Thus, the resolution of the video record is primarily a function of the quality of the X-ray image. The video image is fed into a digital video processor*** device to allow frame averaging and filtering of the signal. The processed record is then recorded on video cassette tape. For these tests, optimum contrast (film density) difference between two X-ray intensity levels was obtained when the device averaged 16 frames at a time.

Thermocouple data were recorded using two eight-channel transient digitizers operating at 100-mV full-scale range and a sample rate of 250 milliseconds per point. The resolution of the vertical and horizontal amplifiers is 25 microvolts and 0.5 milliseconds, respectively. The total record time at this sample rate is 76.4 seconds.

---

*Varian Associates, Palo Alto, CA.

**N. V. Optisele Industrie De Oupe Delft, Delft, Holland.

***Quantex Corporation, Sunnyvale, CA, 94086.

## III. Experimental Observations

### A. Test Sequence

After assembly of the apparatus, the X-ray source was activated and the video record optimized by adjusting both the frame-averaging rate and X-ray voltage. The picture of the particle bed without the thermite provided a very sharp contrast of the bed boundaries. The predicted influence of the thermite melt (change in areal density) was estimated and the source voltage adjusted accordingly. The thermocouple recorders and the video recorder were started approximately 3 minutes prior to test initiation to obtain baseline data.

The test sequence was started by passing an electrical current through the pyrofuse igniter. The thermite reaction began immediately (as indicated by an embedded thermocouple near the ignition point) and proceeded downward through the thermite mixture. The first observation of melt in the X-ray image occurred 35 seconds after ignition, giving an estimated average burn front velocity of 0.8 cm/sec.

The resolution of the field of view of the video X-ray image was not adequate to calculate the velocity of the falling stream. If only gravity were acting, the calculated velocity value would range from 2.7 to 1.8 m/second, depending on the height of the melt pool. Gas pressure within the melt generator may have augmented the velocity if venting was incomplete. If the diameter of the stream were known, the velocity could also be calculated from the rate at which the pool depth increases. Values obtained in this manner range from 0.2 m/sec for a 1.5-cm-diameter to 1.8 m/sec for a 0.5-cm-diameter stream. Melt delivery was completed within 14.7 seconds after initiation. Assuming a constant flow rate, this time gives velocities of 0.7 m/sec and 5.9 m/sec for the 1.5-cm- and 0.5-cm-diameter streams, respectively. Remaining events in the experimental sequence are outlined in Table I.

### B. Test Observations

The video record obtained during the test was processed to improve the contrast between the melt and the particle bed regions. Figures 7 through 14 are a series of photos taken from the video record to illustrate the melt penetration behavior. The time indicated on each photo (in seconds) is referenced to the initial contact of the melt with the bed. The original time in the upper left corner was obliterated during the image enhancement process. The horizontal lines seen in some figures are interference bars that occur during the freeze-framing process.

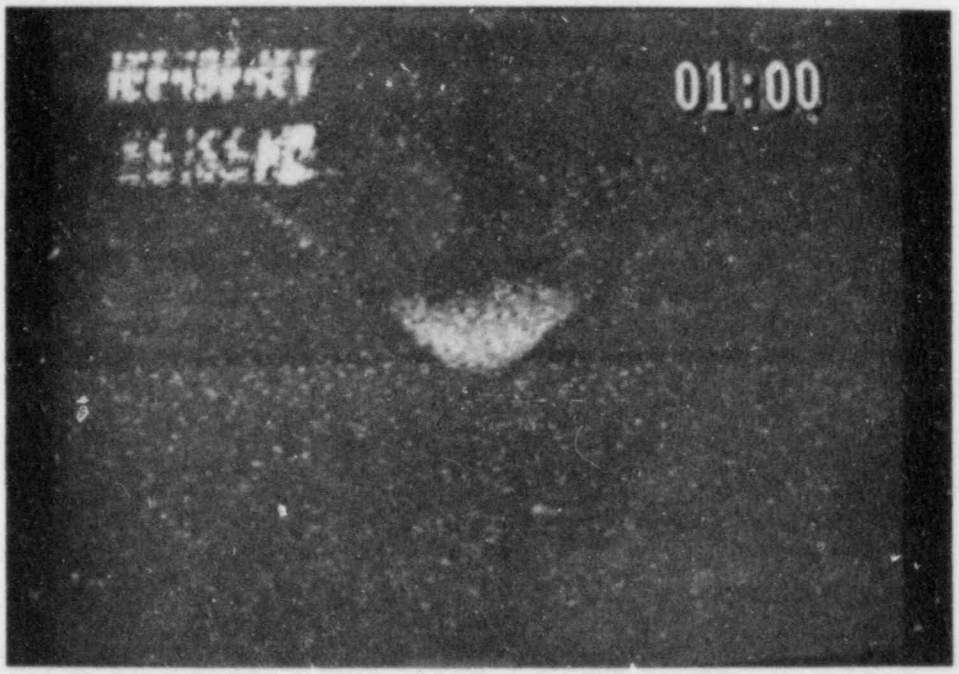


Figure 7. Photograph of Image-Enhanced Video X-Ray Record (Time = 1.0 Sec) (Time in upper right is referenced to melt contacting particle bed. Bright image is the melt formed into the apex of particle bed. View into the paper is parallel to intersection of the two planer surfaces)

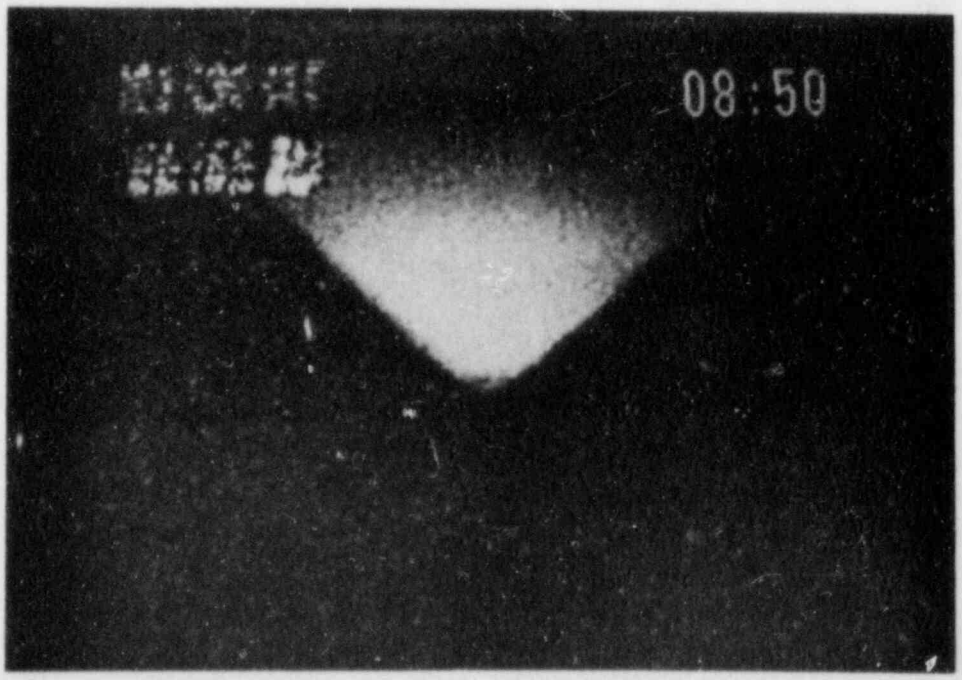


Figure 8. Photograph of Image-Enhanced Video X-Ray Record (Time = 8.5 Sec) (Melt depth is 8.3 cm. Upper edge of melt and melt stream are seen in upper part of picture. Particle bed profile is clearly discernible)

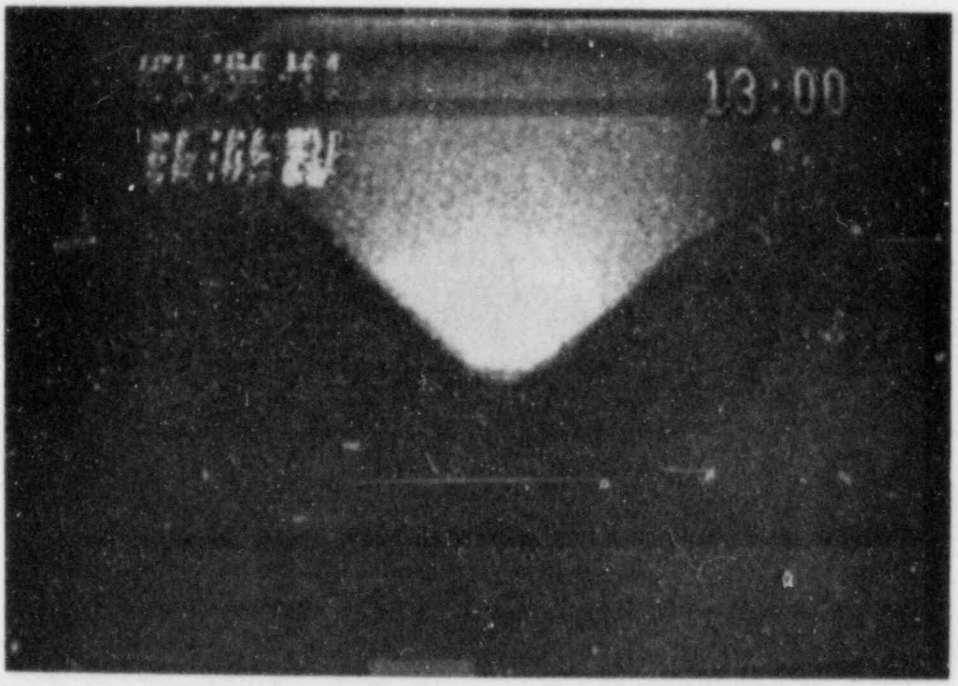


Figure 9. Photograph of Image-Enhanced Video X-Ray Record (Time = 13.0 Sec) (Melt Depth 10.3 cm; melt stream no longer apparent. Contrast change at melt/bed interface is apparent, possibly due to melting of iron oxide particles)

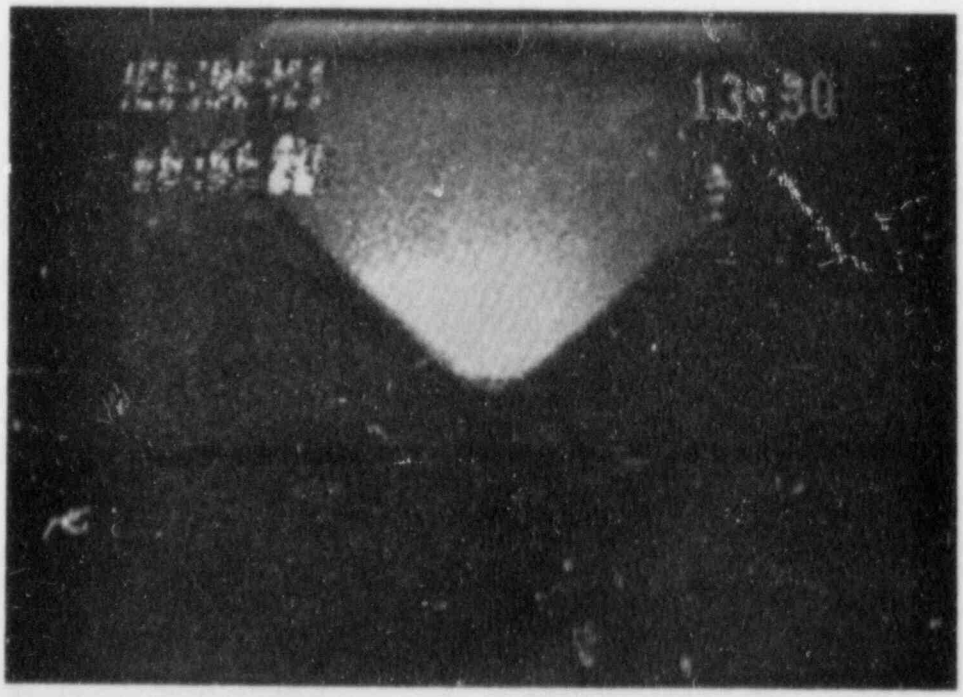


Figure 10. Photograph of Image-Enhanced Video X-Ray Record (Time = 13.3 Sec) (Rapid penetration of bed center is noted. Contrast density of penetration suggests material is molten)

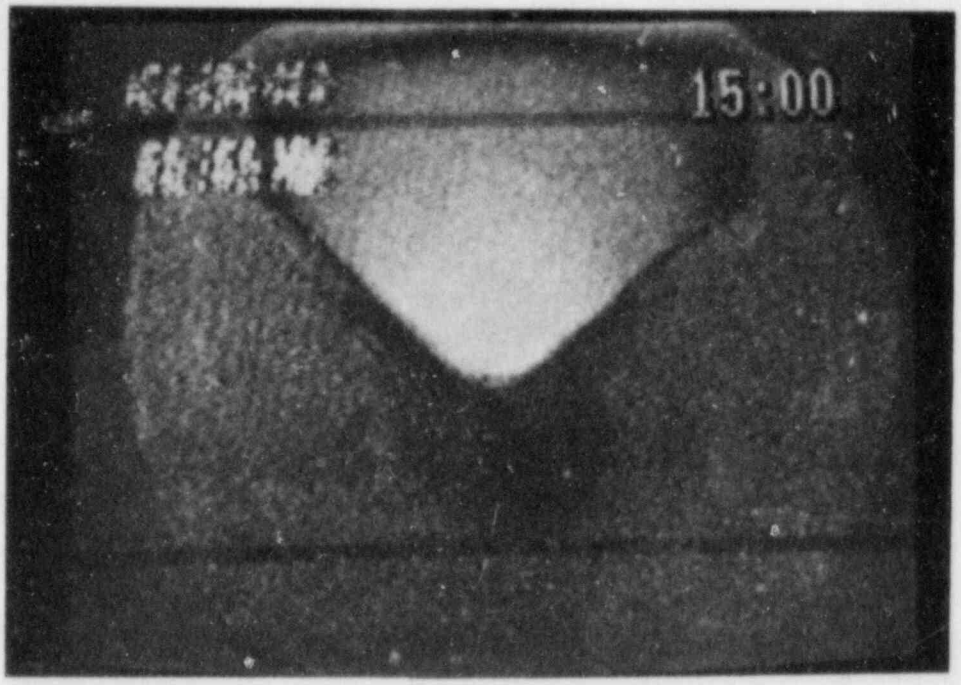


Figure 11. Photograph of Image-Enhanced Video X-Ray Record (Time = 15.0 Sec) (Contrast density shift apparently due to solidification of penetration front. Depth of maximum penetration approximately 4.6 cm)

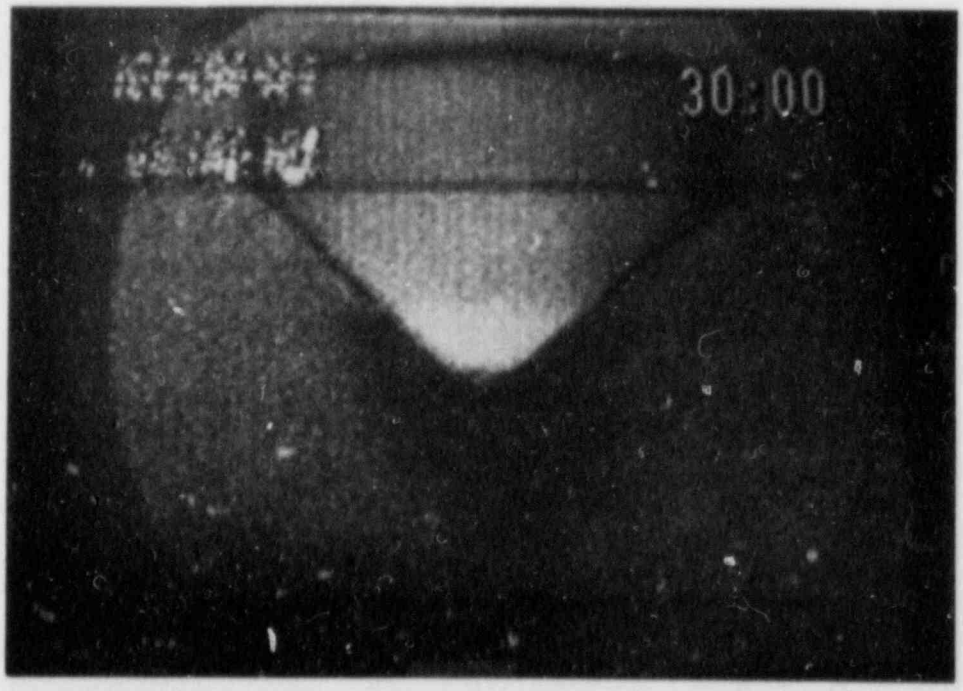


Figure 12. Photograph of Image-Enhanced Video X-Ray Record (Time = 30.0 Sec) (Melt penetration broader and deeper. Level of melt pool has dropped approximately 0.8 cm)

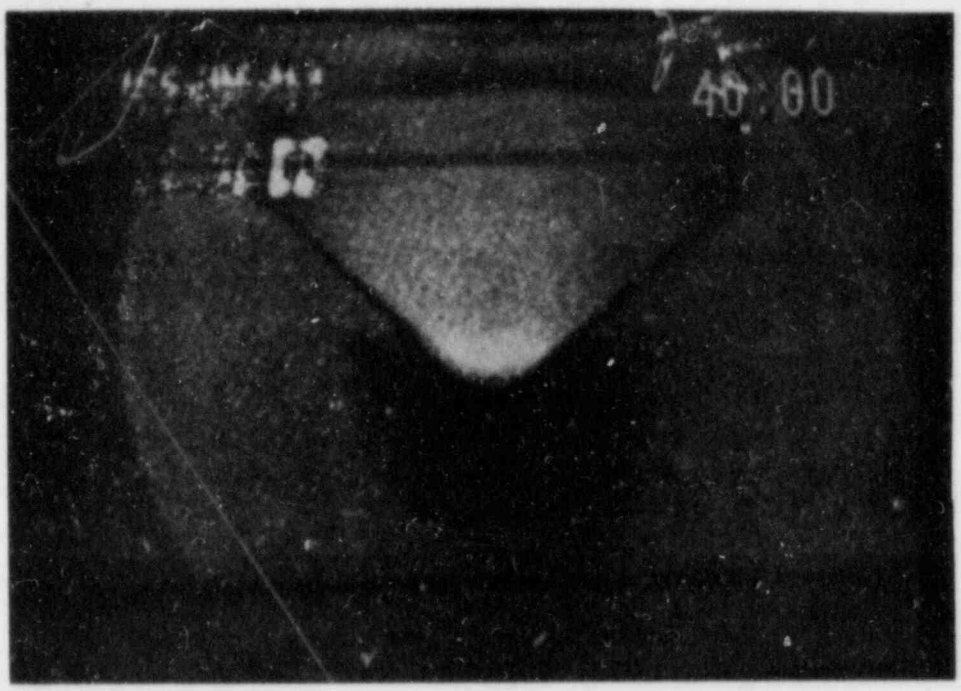


Figure 13. Photograph of Image-Enhanced Video X-Ray Record (Time = 40.0 Sec) (Continual penetration no longer apparent. Crust layers on crucible wall are obvious above melt.)

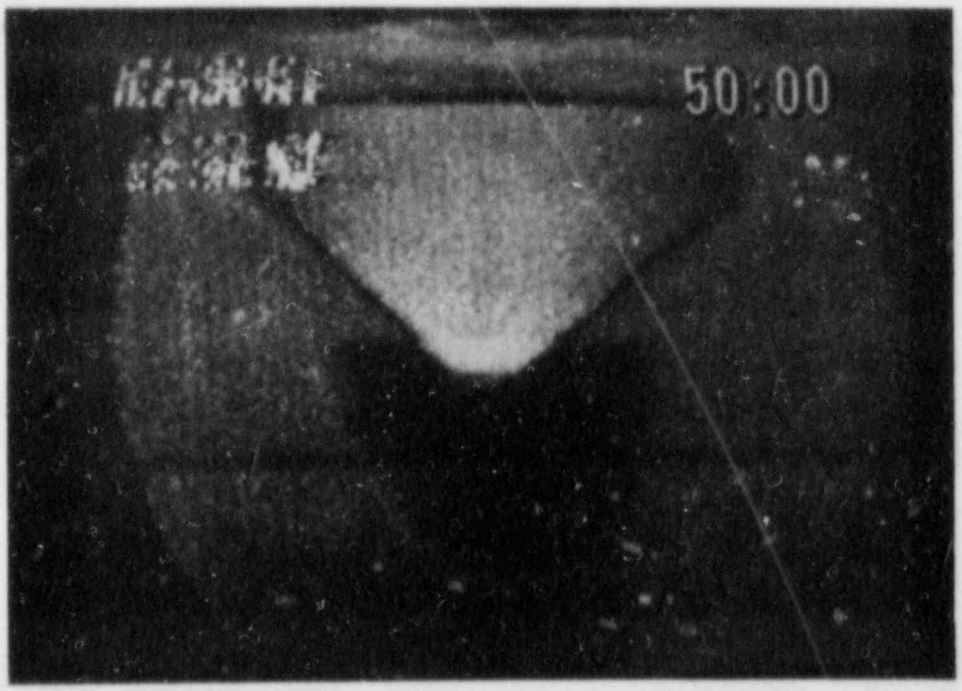


Figure 14. Photograph of Image-Enhanced Video X-Ray Record (Time = 50.0 Sec) (Final shape of penetration is seen. Additional crust formations are noted. Stratification between iron and alumina phases is not obvious due to enhancement process)

**TABLE I**

Events in the PARTICLE BED II Experimental Sequence

| Time (sec) | Event Description |
|---|---|
| 0.0 | Ignition |
| 35.0 | Melt contacts particle bed; density change noted in bed to depth less than 1.0 cm |
| 46.4 | Melt stream ceases; penetration 1.7 cm |
| 48.0 | Rapid penetration begins |
| 50.0 | Penetration appears to stop, depth 5.7 cm |
| 74.0 | Melt stratifies into metallic and oxide phases. Gas bubbles in oxide cease; crust layer forms above melt |
| 75.0 | Final penetration depth (7.0 cm) achieved |

As noted in Table 1, the X-ray image detected an immediate density change in the particle bed to a depth less than one centimeter. The original trough geometry was discrenible during this period, indicating that the melt stream did not immediately penetrate into the bed. The bed particles in this region are assumed to have melted upon contact with the molten pool, but the depth of the zone suggests that the energy in the molten thermite was insufficient to overcome the large heat sink provided by the "cold" particle bed. The X-ray image of this 1.0-cm region is unlike that observed later when melt penetration is obvious. The appearance suggests the material is less dense than liquid iron, possibly a molten mixture of iron oxide and iron or molten iron oxide alone.

Approximately 13 seconds after the melt contacts the bed, rapid penetration occurs. The actual penetration depth as a function of time is difficult to discern because of the unsharpness of the image and the necessity to resolve a three-dimensional figure from a two-dimensional image. Figures 9 through 11 show the progression of the melt over the time period from 13.0 to 15.0 seconds after the melt contacts the bed. Obviously, the penetration proceeds at a very rapid rate. The penetration rate may be enhanced by the heating of the particle bed that occurs while the melt pool is stopped at the original bed interface. With the temperature of the particles elevated, the amount of energy absorbed from the melt as it penetrates is decreased.

The rapid melt penetration appears to stop at about 15 seconds, and is followed by a more gradual penetration at later times. This behavior suggests that the movement of the melt is dependent upon the temperature difference between the melt and the bed. For example, the initial melt contact results in freezing of the melt or the melting and freezing of a portion of the iron oxide due to the large amount of heat absorbed by the bed. The period following allows more energy to leave the melt and enter the bed, causing the particle temperature to increase. As the temperature difference across the interface decreases, the iron or the iron oxide again liquifies and bed penetration begins. This process can occur rapidly because the iron oxide is at a high temperature. The melt continues downward until a point is reached where the particle temperature is too low to allow melting to occur, and the penetration is halted.

The process of freezing, heating, and melting is repeated later in time to cause additional penetration. The extent of the process steadily decreases because less energy is available in the melt during each successive cycle. The maximum depth of penetration from the original bed elevation is estimated to be 7.0 cm. Figures 12 through 14 illustrate the additional melt penetration that occurs after 15 seconds.

Figure 15 plots the penetration depth as a function of time to illustrate the process described above. The data points represent the maximum extent of the melt at the time in question. Two time scales are shown: one for the period from melt deposition through 60 seconds; the second time scale is given from 12 to 15 seconds, to show the rapid movement that occurs over this period. The uncertainty in these data could be as large as 20%, caused by the lack of sharpness and clear contrast in the video record. As indicated above, most of the penetration (5.0 cm) occurs over the time frame from 13 to 15 seconds.

## C. Posttest Examination

Figures 16a and 16b are graphic reconstructions of the observations made during posttest X-ray and disassembly of the apparatus. Cross-sectional views in two orthogonal planes are given to illustrate the geometric characteristics of the melt penetration. A clear demarcation between the oxide (alumina) and metal (iron) phases of the melt is confirmed by the observation of melt stratification in the X-ray record. A thin dome or crust layer of alumina, spanning the entire crucible, is located 2.5 to 3.8 cm above the major portion of the alumina phase. A thin layer of the same material also covers the vertical sidewall between the dome layer and the upper surface of the alumina phase. Sectioning of the alumina phase shows a large number of voids, apparently caused by trapped bubble formation attributed to emerging gases.

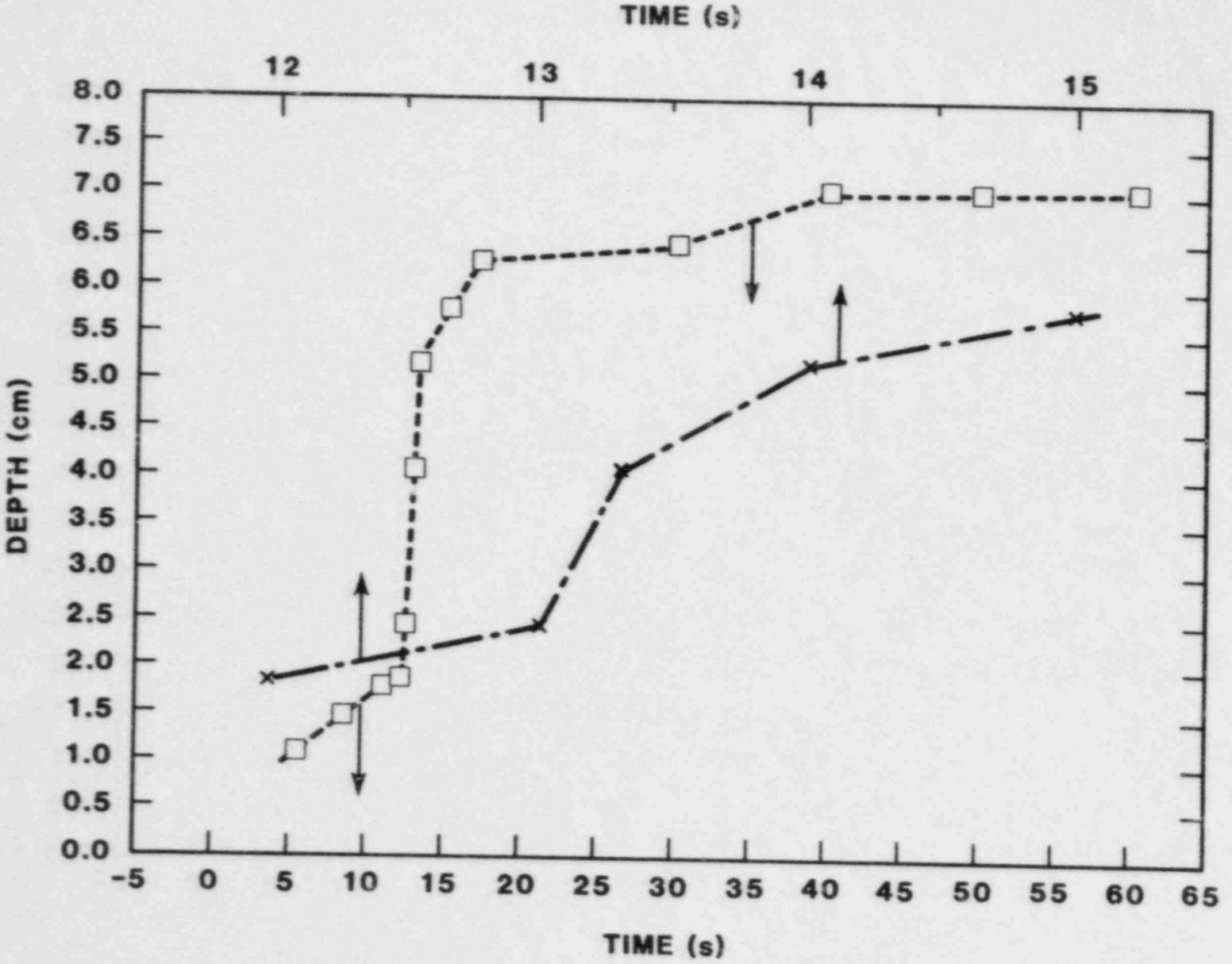


Figure 15. Melt Penetration into Iron Oxide Particle Bed

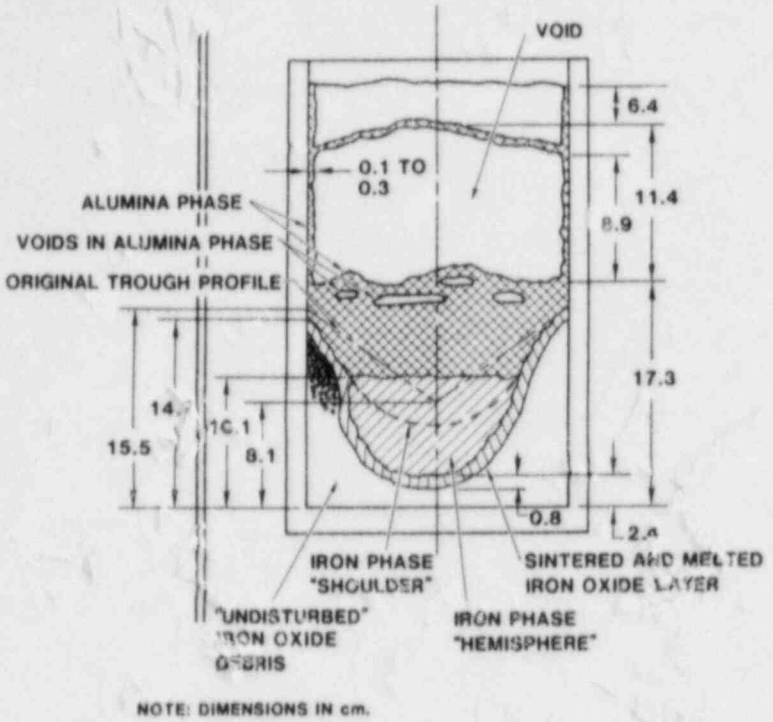


Figure 16a.

Posttest Front Profile for PARTICLE BED II Experiment

DIMENSIONS IN cm.

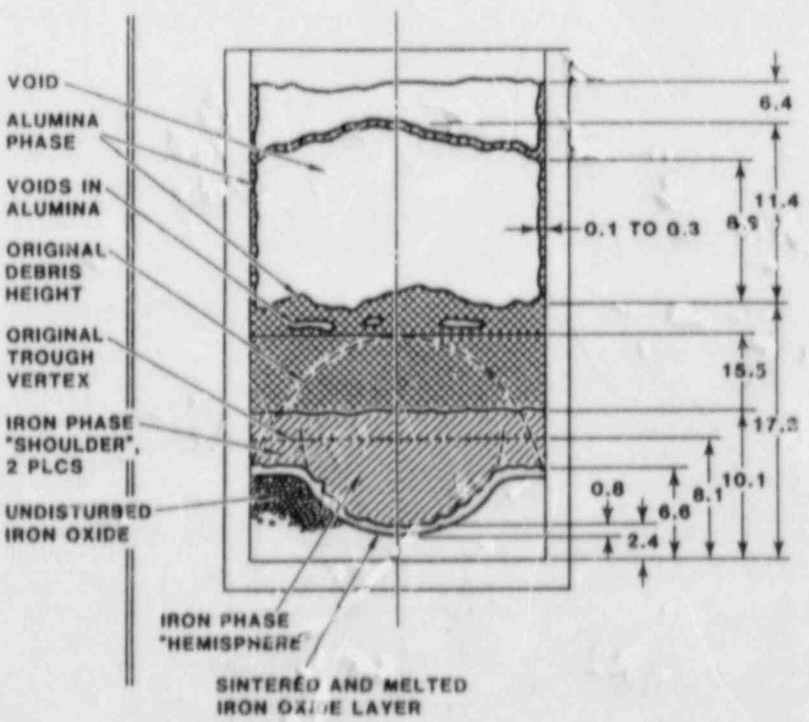


Figure 16b.

Posttest Cross-Sectional Side Profile for PARTICLE BED II Experiment

The metallic (iron) phase is separated from the alumina phase by a number of large voids at the interface between the two materials. The shape of the iron is described as a segment of a horizontal cylinder lying along the original vertex of the bed trough, with a spherical shape emanating from the center of the length. Figure 17 shows a photograph of the cross-section of the iron and alumina shapes to help describe the geometry. The dome-like crust was destroyed during the sectioning operation, but the alumina frozen on the crucible sidewalls is evident in the photograph. The large voids in the alumina phase are concentrated near the upper surface of the phase. A void between the iron and alumina phases is also apparent. Two views of the sectioned iron phase are given in Figure 18. The machined surface (Figure 18a) shows a dense structure with only isolated voids. The surface of the iron in contact with the particle bed (Figure 18b) is nearly smooth with no obvious melt "fingers", as would be expected if the melt had flowed through the channels between particles. Metallographic analysis of the iron is given in a subsequent section.

The masses of alumina and iron phases were measured after recovery from the apparatus. Results are given in Table II for the PARTICLE BED I and II tests, together with the expected mass from a stoichiometric analysis of the reaction.

The data of Table II show that both the iron and alumina phases are heavier than would be expected from the products of the thermite reaction. For the temperatures experienced during the tests, iron oxide is soluble in both iron and alumina, with a positive driving force toward the alumina phase. Iron oxide in alumina can form hercynite, $FeAl_2O_4$, or the solid solution $(Al, Fe)_2O_3$. The small change in mass noted for the iron phase is attributed to iron oxide "trapped" during the solidification of the iron.

**TABLE II**

Mass of Alumina and Iron Phases

| | | Mass | | |
|---|---|---|---|---|
| | | Stoichiometric Analysis | Test Sample | Percent Diff(%) |
| PARTICLE BED I | Alumina | 4479.5 | 7325 | 63.5 |
| | Iron | 5520.5 | 6000 | 8.7 |
| PARTICLE BED II | Alumina | 4479.5 | 7800 | 73.7 |
| | Iron | 5520.5 | 6025 | 9.1 |

Figure 17. Photograph of Sectioned Alumina and Iron Phases

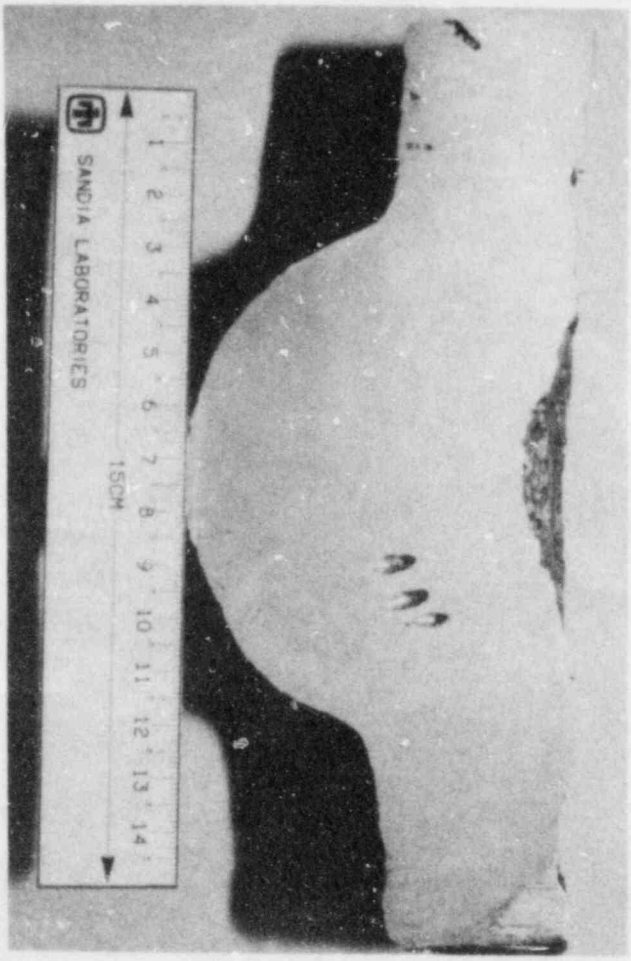


Figure 18a. Photograph of Sectioned Iron Phase Showing Interior Structure

Figure 18b. Photograph of Sectioned Iron Phase Showing Outer Surface

The geometry shown in Figure 16 indicates that the iron and a portion of the alumina are occupying regions that were originally part of the particle bed. The volume represented by these regions has been calculated to determine the mass of iron oxide removed. Table III gives the results of these calculations.

**TABLE III**

Mass of Displaced Iron Oxide

| Test | Total Mass Gain (g) | Calculated Displaced Volume ($cm^3$) | Equivalent Iron Oxide Mass (g)* |
|---|---|---|---|
| PARTICLE BED I | 3335 | 1070 | 3253 |
| PARTICLE BED II | 3805 | 1135 | 3450 |

*Based on 3.04 $g/cm^3$

The agreement between the mass gained and the calculated mass in the displaced volume is good considering the lack of precision in the dimensional measurements. The results suggest that most of the iron oxide removed from the bed went into solution with the iron and alumina.

The portions of the melt (both alumina and iron) in contact with the particle bed are covered with a coherent layer having the appearance of melted and sintered iron oxide particles. A gap, probably caused by shrinkage of the iron during cooling, separates the iron and the iron oxide layer. Photomicrographic and X-ray dispersive analyses of this approximately 0.8-cm-thick layer are given in a subsequent section.

## IV. Results and Discussion

### A. Metallography of Iron Phase

Quarter-section slices taken from the iron phases recovered from both experiments are used to determine the grain and void structure. Each 1.3-cm-thick specimen was polished and then etched with 2% nitric acid in alcohol to accentuate the grain boundaries. Figure 19 shows the section obtained from PARTICLE BED II. Macroscopic inspection reveals only a few isolated defects such as the void in the lower left corner of the sample. No large-scale impurities or segregation of elements can be seen. Two subsequent figures (20 and 21) at higher magnification (25X) show comparison of grain size in regions near the periphery and center of the sample. Grain size within a material's structure can be used to imply the cooling rate of the sample (Ref 5). Larger grains are associated with slower cooling of the material from an equilibrium transition temperature. Inspection of the photos shows some grains to appear darker than others and some adjacent grains have micrograins while others do not. Both of these effects are attributed to the crystallographic orientation of the grain with respect to the polishing plane of the sample; this orientation causes differing diffraction patterns of the illumination.

Grain-size numbering is normally done using grain counts obtained from photomicrographs taken at 100X. For other magnifications, a correction factor (Q) can be obtained from:

$$Q = 6.64 \log_{10} (M/M_b) \qquad \text{(Ref 6)}$$

where

$M$ is the magnification used, and
$M_b$ is the standard magnification (100X).

From Figures 20 and 21,

$$Q = 6.64 \log_{10} (25/100) = -4 .$$

Thus, for 25X magnification, the true ASTM grain size number is 4 numbers lower than that obtained from the photomicrograph. The grain size index of Figures 20 and 21 is estimated by comparison to a standard comparison chart given in Ref 6. The sample presented in Figure 20 compares best to grain size 3 (untwined grains). The resulting true ASTM index is then 00 (-1), with an average grain "diameter" of 0.51 mm. In terms of steel-making technology, grain index numbers less than 4 are considered to be coarse-grained (Ref 7). The large grains suggest that the mate-

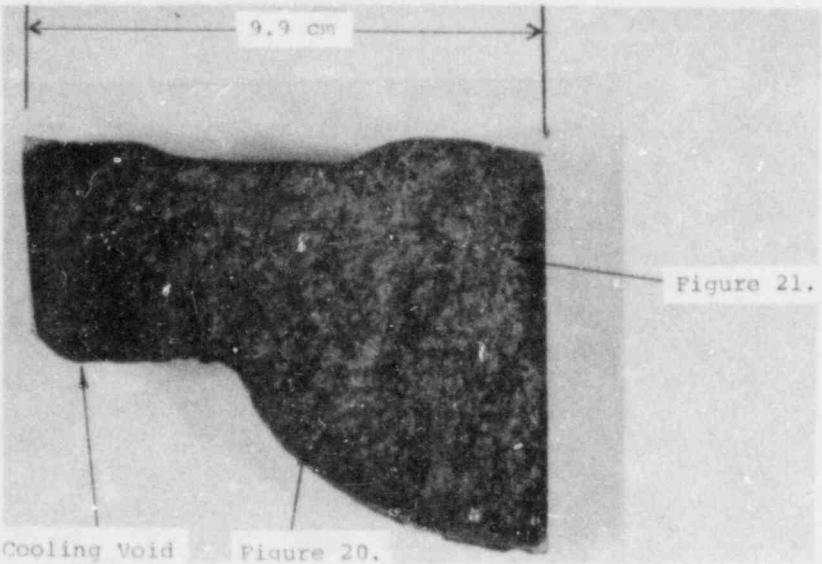


Figure 19.

Photomicrograph of Polished and Etched Quarter Section of the Metallic Phase from PARTICLE BED II

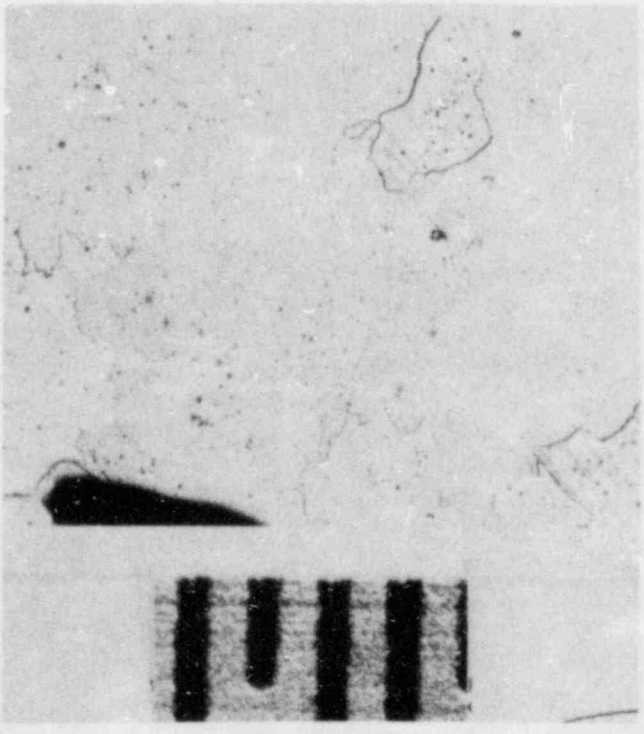

Figure 20.

Photomicrograph (25X Magnification) of Region Near the Periphery of the Iron Phase (Length scale divisions are 0.5 millimeter)

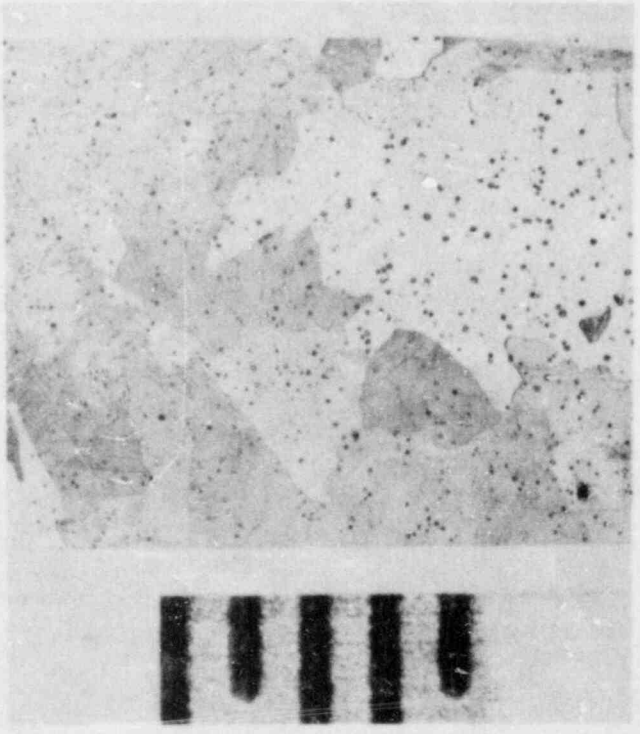

Figure 21.

Photomicrograph (25X Magnification) of Region Near the Center of the Iron Phase (Length scale divisions are 0.5 millimeter)

rial near the boundary was at high temperature (i.e., at or above transition) and the cooling rate was slow, comparable to that experienced with furnace or air cooling.

The grain structure from the central region of the iron (Figure 21) is slightly less coarse than that of the material at the periphery. The material in the central region of the iron phase has nearly the same grain size index as that seen at the boundary region. Both regions appear to have cooled at nominally the same rate, implying that the exterior of the iron (in the area described by Figure 20) did not freeze in a time span short enough to cause termination of the penetration. Thus, the assumption that the heat transfer to the particle bed was adequate to cause solidification of the outer iron boundary is not supported by the grain structure results. The melting and then freezing of the iron oxide in contact with the iron may then have been the mechanism halting penetration.

Comparing the micrographs from the two regions provides an indication of how the iron solidification proceeded. The small, dark areas evident in both photos are attributed to impurities in the iron or entrained gas. The frequency of these small regions is significantly higher in the more central portion of the iron (Figure 21). The higher concentration is attributed to migration of material gases out of solution as the iron cooled. Assuming the iron cooled from the outer boundaries inward, the impurities would tend to migrate to the central area and be "trapped" as the material froze. Freezing from the outside-to-inside is also expected intuitively from heat transfer considerations, considering the large radiative and conductive surface areas provided by the crucible and particle bed.

B. Metallography of Iron Oxide Layer

A portion of the coherent layer found next to the solidified melt was analyzed using a technique similar to that described for the iron specimen. Figure 22 is a photomicrograph of a section of this layer taken at 6.3X magnification. The surface closest to the iron (upper edge in Figure 22) contains a large number of depressions caused by gas trapped between this layer and the iron phase. The occurrence of these "pockets" suggests that the material in this region solidified, preventing gas diffusion through the bed. As Figure 22 shows, the gas bubbles do not appear to extend in depth beyond two millimeters. Apparently, gas diffusing beyond the 2-mm limit was able to pass through the remainder of the particle bed.

The layer shown in Figure 22 can be described as being composed of a number of distinct phases. Those areas closest to the iron appear to have melted and then solidified. Concentrations of light-colored material are obvious. The central region shows a transition from the fully melted material to a phase that

retains some of the particle structure. Subsequent photomicrographs present these areas at high magnification to show their structural details.

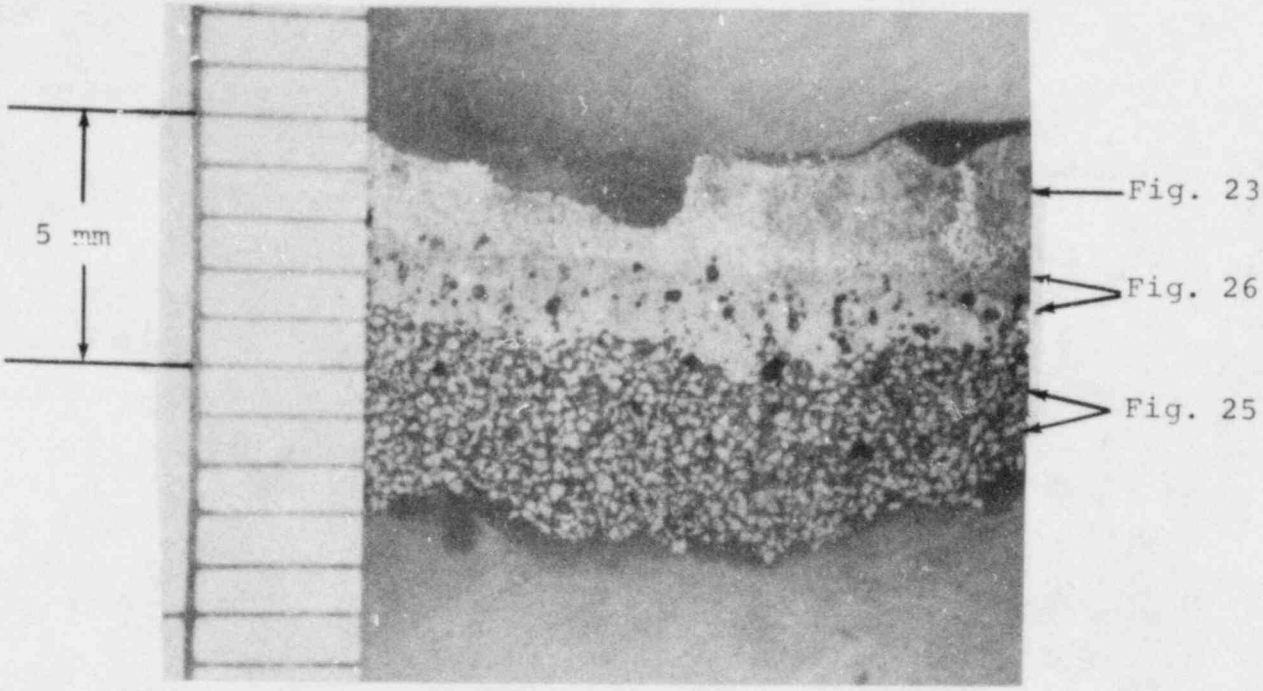


Figure 22. Cross-Sectional Photomicrograph of Coherent Iron Oxide Layer Found Between the Iron Phase (Above) and Undisturbed Iron Oxide Particle Bed (Below) (Magnification of 6.3X)

Figure 23 is a photomicrograph at 100X magnification of the region that was closest to the melt. Three distinct shadings are obvious in the figure: white, gray and black. The results of an energy-dispersive X-ray analysis are given in Figure 24. This analysis indicates that all three areas are dominated by the element iron. The different shading of the light and gray areas results from light diffraction of the grains slightly tilted from the viewing surface. The temperatures required to achieve this structure are sufficient to cause reduction of the iron oxide to elemental iron. The X-ray analysis appears to be a good representation of the actual material in this region.

The dark area, however, does not show as strong an Fe (iron) peak as the light or gray areas and has some impurities in the form of aluminum, silica, and manganese. The dark areas may then be considered as concentrations of the impurities inherent within the iron oxide material used to form the particle bed.

Based on these observations, the penetration of the iron into the particle bed was terminated by the freezing of the iron

oxide in contact with the melt. This assumption is supported by the apparently consistent cooling rates inferred for the iron phase as a whole.

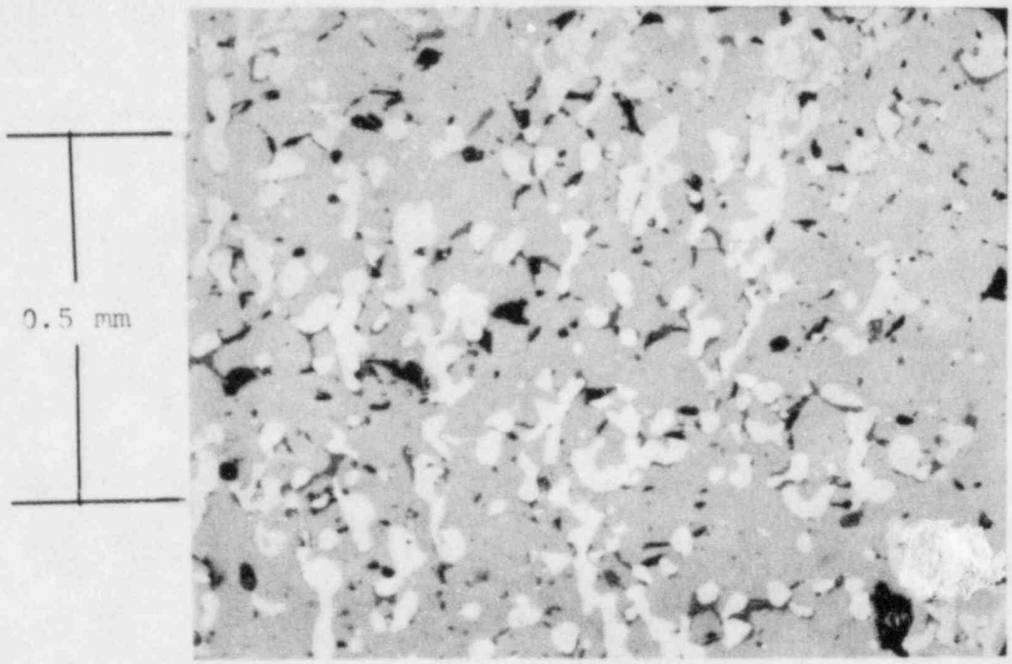


Figure 23. Photomicrograph of Coherent Iron Oxide Region Closest to the Iron Phase (Magnification of 100X)

Figure 25(a & b) shows the transition from the region directly in contact with the iron phase to the outer part of the coherent iron oxide layer. The change in the grain structure is apparent from the large grain-size in these figures relative to that seen in Figure 18. The apparent absence of the light areas is the result of the larger grains being polished to the same surface elevation. The large grain size and lack of voids suggest the cooling rate was slow enough to permit the entrained gas to diffuse out of the region. The gas remaining in the region appears to have coalesced into the large, isolated voids seen in the lower portion of Figure 25b.

Figure 26(a & b) shows the region of the coherent layer located farthest from the iron phase. Figure 26a illustrates the transition area between the two regions where extensive particle sintering has occurred. The flow of material among the individual particles is responsible for the bond strength inherent in this region. The individual particle shapes (apparent in Figure 26b) are similar to those seen in Figure 5. Voids are seen within all of the spherical particles shown in the figures and are assumed to be formed during manufacture. The shape of the particles suggests that the material flow occurs at the outside

(a) Light Area

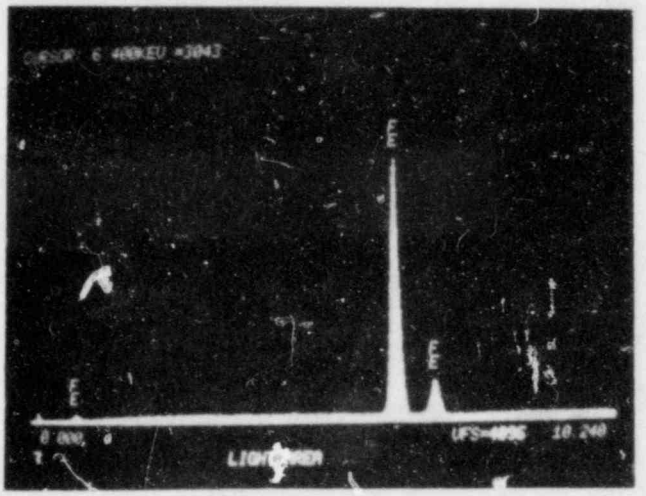

(b) Grey Area

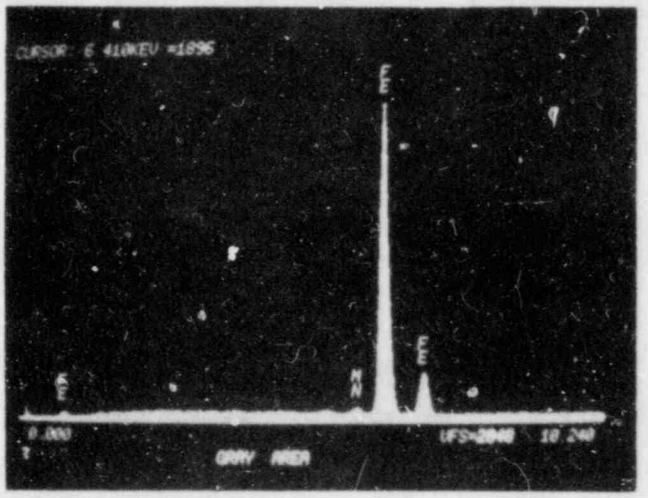

(c) Dark Area

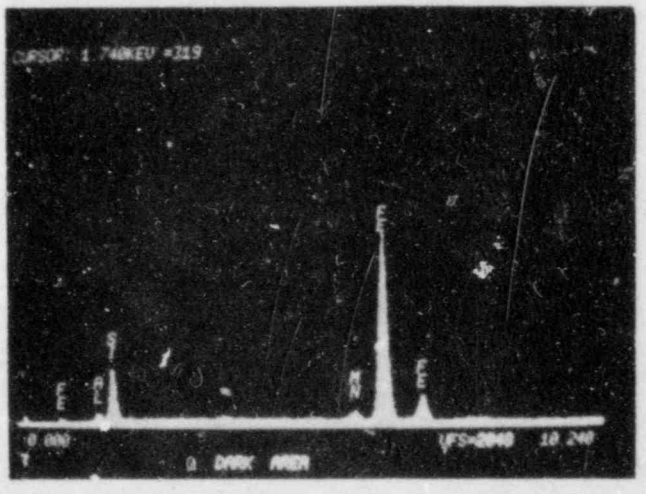

Figure 24. X-Ray Analysis of Coherent Iron Oxide Layer Closest to the Iron Phase

(a)

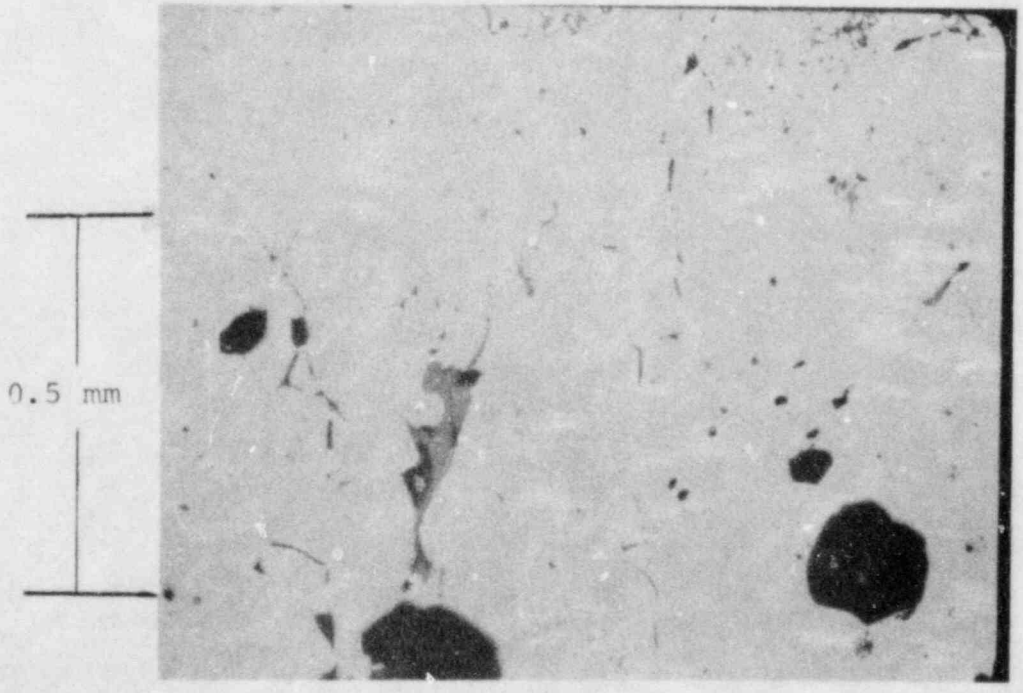


(b)

Figure 25. Photomicrographs of Coherent Iron Oxide Layer Showing Transition Region

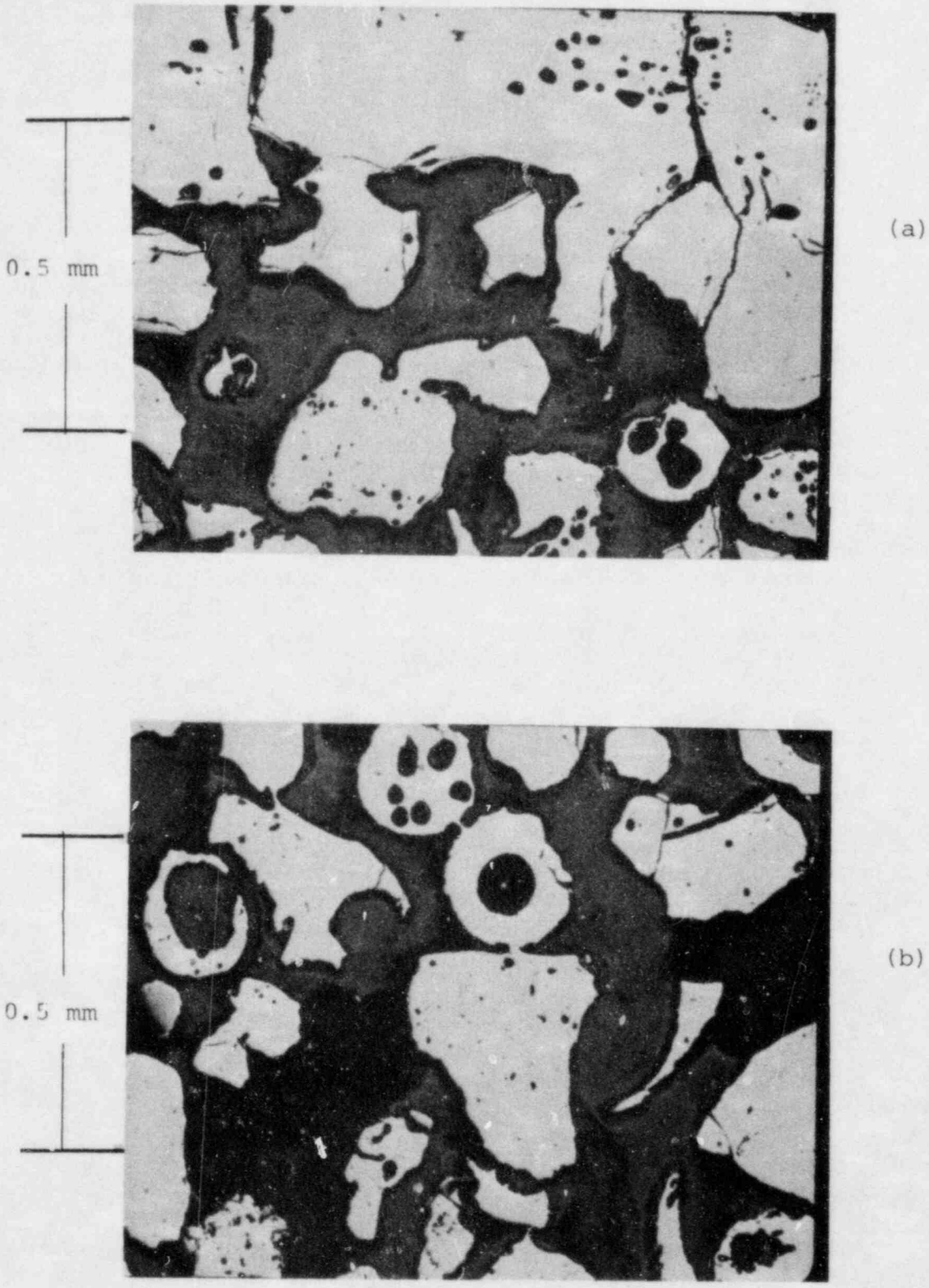


Figure 26. Photomicrograph of Coherent Iron Oxide Layer Showing Region of Sintered Particles

surface of the individual particle with the extent of sintering determining the final size. The relative size of the particles through this region indicates that the extent of sintering decreases with increasing distance from the iron-phase interface.

C. Metallography of Alumina Phase

Metallography was performed on a portion of the alumina phase from PARTICLE BED II. Figure 27 is a photomicrograph of the sample taken at 100X magnification. Three regions are apparent; two distinct phases (light and dark in Figure 27) and an interstitial ground mass (appears gray in Figure 27). Elemental analysis by electron microprobe analysis of this region is given in Figure 28(a, b, c). The analysis shows that aluminum (Al) is apparent in almost all regions except the small, isolated dark areas. These small regions are probably voids within the matrix of the material. The probe analysis for iron (Fe) shows that the dark areas of Figure 27 are virtually all aluminum. These observations suggest that the dark regions are corundum ($Al_2O_3$) and the light areas are composed of hercynite ($FeAl_2O_3$) formed from the absorption of iron oxide particles. The interstitial areas show concentrations of silica (Figure 28c) and iron and an absence of alumina. Higher magnification (400X) photomicrograph and microprobe analyses of an interstitial area are given in Figures 29 and 30. The analysis suggests the region to be mostly iron and silica, possibly in the form of iron silicate.

The composition of the alumina phase indicates that the iron oxide particles migrated through the iron phase to form hercynite. The impurities in the phase segregated into interstitial regions composed mostly of iron and silica. The grain structure in the region studied appears to be large and inconsistent with a number of voids. The frequency of the voids increases near the outer boundary and upper surface. This behavior implies that these regions froze quickly and trapped the emerging gases. The relatively slow cooling of the more central region probably allowed the gas to diffuse to the phase boundaries.

D. Iron Oxide Particle Size

The thermal energy of the deposited melt has the potential to induce temperature gradients within the individual particles. These gradients can then cause thermal stresses that may initiate particle fracture. The effects of particle fracture are twofold; one, the number of flow channels will increase and the relative size of the individual channel may decrease (i.e., by closer packing of particles). Two, the volume-to-surface-area ratio will decrease as the particles become smaller, causing the particle's heat capacity relative to exposure area to become smaller.

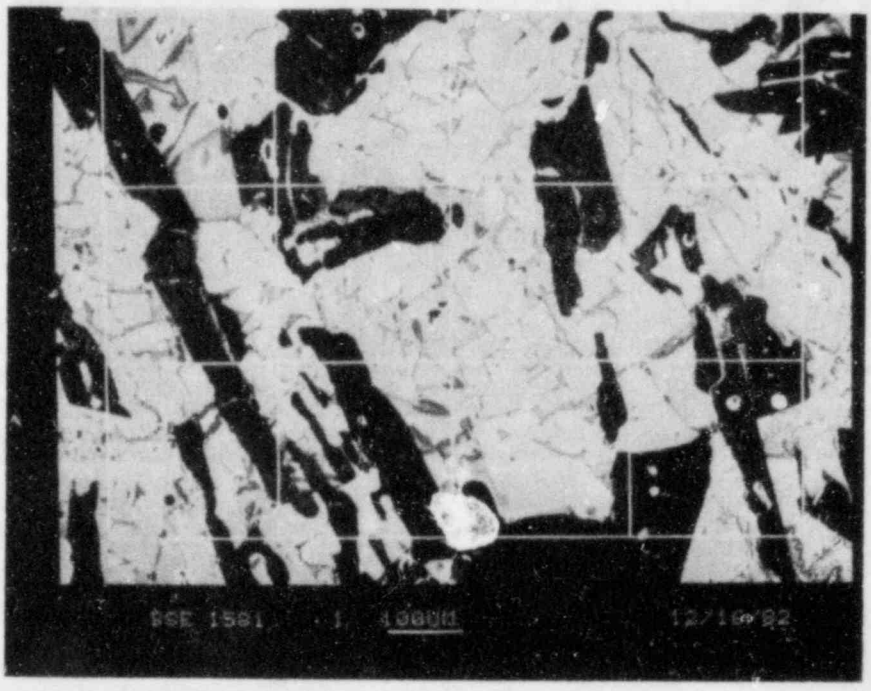


Figure 27. Photomicrograph at 100X Magnification of a Portion of Alumina Phase

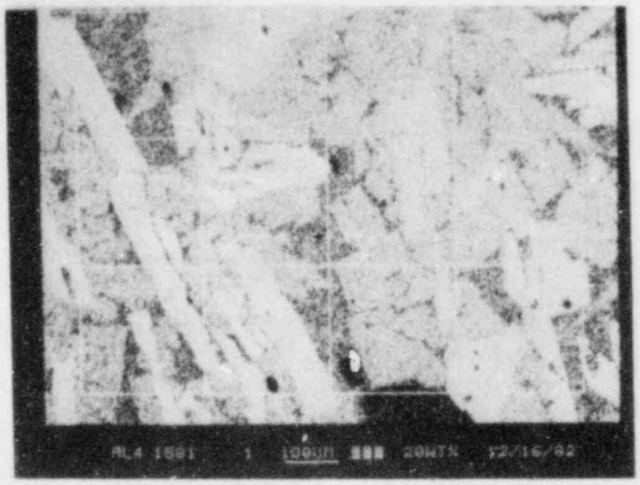

(a) - Aluminum (Al)

(b) - Iron (Fe)

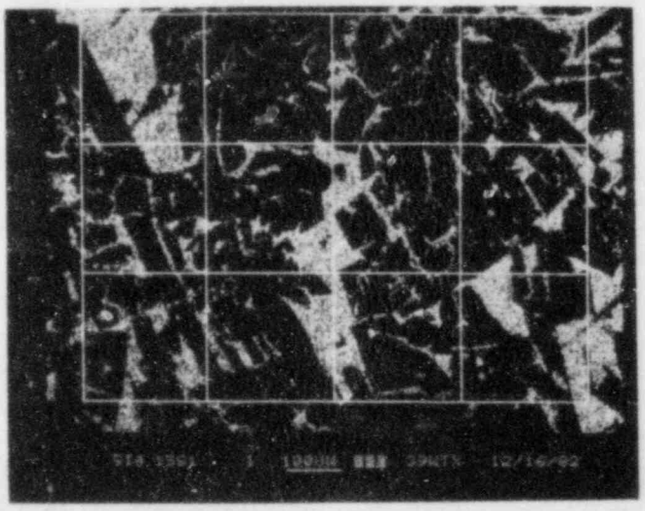

(c) - Silica (Si)

Figure 28. Electron Microprobe Analysis of Alumina Phase Region

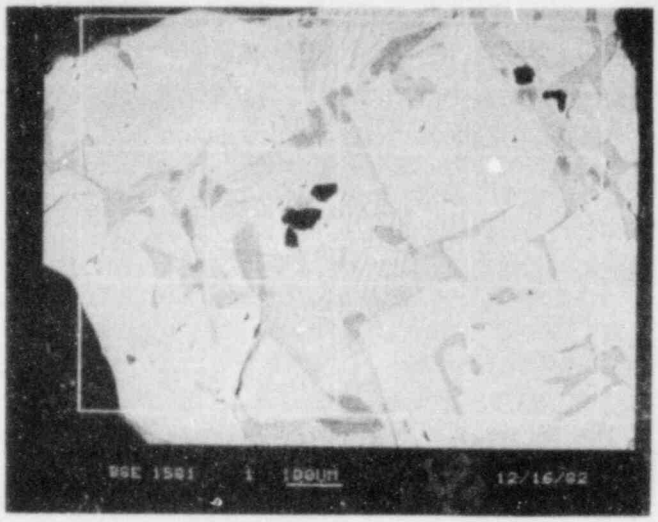


Figure 29.

Photomicrograph at 400X Magnification
of Interstitial Area of Alumina Phase

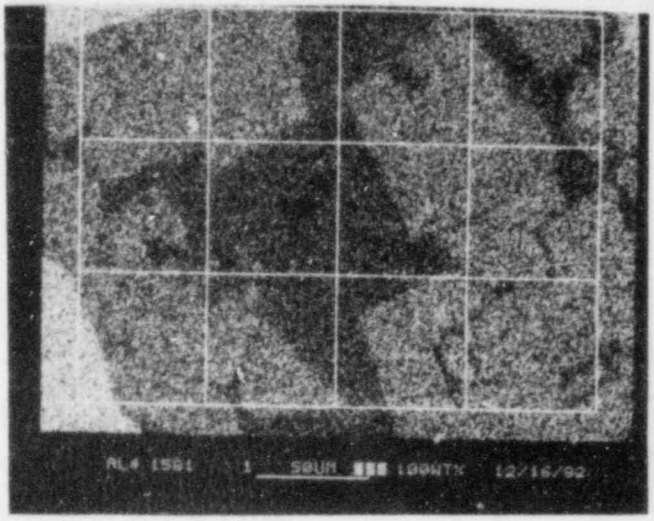


30(a) - Aluminum (Al)

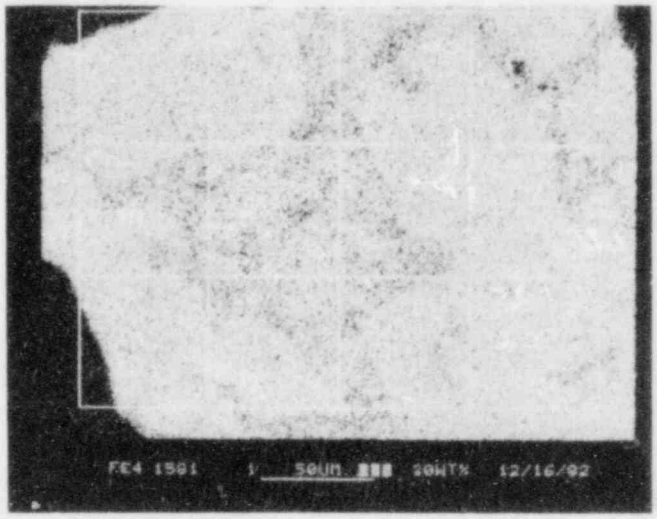


30(b) - Iron (Fe)

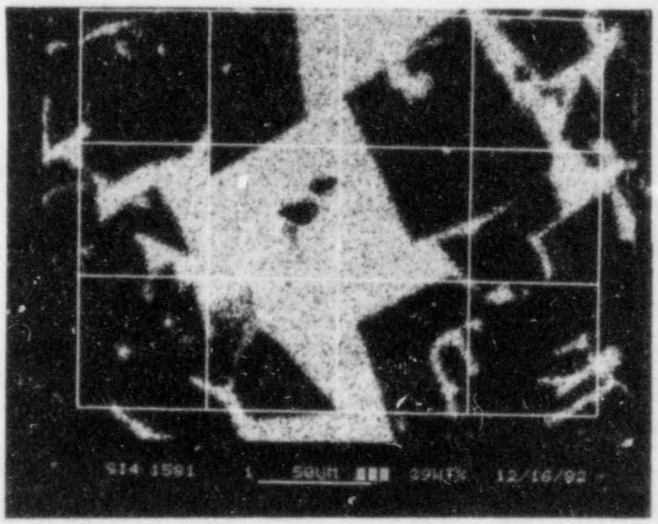


30(c) - Silica (Si)

Figure 30.

Electron Microprobe Analyses
of Interstitial Area

The net result will be faster heat transfer to the particle and possibly more rapid freezing of the melt. However, if heat transfer within the bed improves, the heat flux to the surrounding concrete structure may increase. In a situation where coolant is to be added, retaining larger particles at the periphery of the bed structure may be desirable. The two effects of particle fracture indicate that creating smaller particles may have a net beneficial effect on halting the melt penetration, but not on limiting the heat flux to the surrounding concrete structure.

A mechanical sieving analysis of the recovered iron-oxide particle-bed material was performed to determine if the heat fluxes generated during the test caused sintering or fracturing of the particles. Eight sieves were employed with the initial screening (850- m average opening) used to remove large debris and foreign matter from the bed material. No portion of the coherent layer described in Section IV-B was included. The total material screened was 2002.0 and 1997.0 g for PARTICLE BED I and II, respectively. Table IV has the results of the sieve analysis. A Belastung Banjahi shaker, model EML 200, was used, operating for 45 minutes at a setting of 66. Four batches of nominally 500 g each were required to complete each sample.

The particle size results from the two tests are quantitatively similar. Compared to the pretest particle size range, approximately 7.8% of the iron oxide material recovered from the test increased in size. The increase is attributed to sintering of individual particles to form agglomerates of larger size. The quantity of material within the original size range (212 to 355 m) is approximately 90% and 88% for PARTICLE BED I and II, respectively. The majority of the remaining material is found in the range 180 to 212 m, indicating that the amount of the size reduction is small.

**TABLE IV**

Posttest Sieve Analysis of Iron Oxide Particle Bed

| | | Weight Percent (%) | |
|---|---|---|---|
| Sieve* Number | Average Opening Size ( m) | PARTICLE BED I | PARTICLE BED II |
| 45 | 355 | 7.32 | 7.33 |
| 60 | 250 | 60.11 | 49.72 |
| 70 | 212 | 29.90 | 38.33 |
| 80 | 180 | 2.30 | 4.11 |
| 120 | 125 | 0.12 | 0.20 |
| 170 | 90 | 0.02 | 0.10 |
| 270 | 53 | 0.05 | 0.10 |
| Catch Pan | - | 0.17 | 0.10 |

The small amount of apparent particle "fracturing" is not unexpected considering the conditions during the tests. The principle mechanisms for this type of damage are surface tensile stresses induced by a thermal gradient within the particle. Stresses of the magnitude required to cause fracture can generally be created only by a sudden quenching or cooling of a heated material. Thermocouple records and the grain size growth within the coherent layer suggest that the cooling pattern was slow and continuous, apparently providing adequate time for stress equilibration within the individual particles. It is also possible that fracture can occur upon contact with the melt due to the large number of inclusions in the surface of the particles and the complexity of the thermally-induced stress pattern. However, only a small layer of particles at the initial melt interface are thus exposed and these particles are ultimately melted and absorbed.

The limited amount of particle fracture observed in the two tests suggests that prototype beds may not need to be constructed from materials that are resistant to thermal shock. The events in an accident sequence are not characteristically different than the experiments except that the decay heating will be present. The continuing heat source in the core debris will eventually cause the entire bed to be heated. If the bed temperature follows the decay heat history, bed cooling will occur over times sufficiently long to prevent large stress gradients. However,

this will not be the case if coolant is supplied to the bed in an effort to cool the debris. Relatively cool liquids entering the bed (possibly from below the debris) may cause large surface tensile stresses in the individual particles. If the stress gradient is sufficiently large, cracking with subsequent fracture may be induced.

## E. Heat Flux Results

The temperature recorded by the thermocouples placed in the crucible sidewall and base, and in the brick between the upper and lower sections of the apparatus are used to estimate incident heat flux by an inverse heat conduction technique (Appendix B). Figure 3 shows the locations for the thermocouples. The individual thermocouple temperature-time histories are in Appendix A.

An indication of the effect of the particle bed on the incident heat flux can be found by comparing protected and unprotected thermocouple records. Figure 31 shows the temperature-time histories for the top and upper middle thermocouples on both the rear and side planes. The top thermocouples are embedded 1.0 cm from the crucible sidewall and a minimum of 11 cm above the particle bed. The heat flux imposed on these locations is principally radiant energy from the top of the melt pool. Some additional energy was received from the thin shell of alumina that formed on the inside of the crucible. The shell probably formed early in the test when molten material froze on the cold crucible wall. The close agreement of the two top thermocouple records implies that the heat flux above the melt pool was uniform.

The slight difference between the response of the two top thermocouples is attributed to the amount of the alumina material frozen on the crucible wall adjacent to these two locations. Post-test inspection of the crust layer shows it to vary by $\pm 0.5$ cm, depending on radial location. The quantity of crusted material affects the thermal resistance of the layer to subsequent heat transfer via radiation from the molten pool.

The upper middle thermocouples are also in the crucible wall, but the vertical location of the side plane sensor causes it to be protected by a portion of the particle bed. The minimum thickness of the bed adjacent to this thermocouple location is initially 4.0 cm. After the test the protective layer was estimated to be 1.7 cm. The two upper middle thermocouple records are obviously different, both in response time and maximum temperatures. The portion of the particle bed adjacent to the side plane thermocouple causes the peak temperature to be reduced and the time to reach the maximum temperature to increase. The behavior in this comparison suggests that the particle bed is effective in delaying the incident heat transferred and reducing

the ultimate temperature of the embedded structure. Note that the two records are converging at times beyond 1200 seconds. Comparing records for times up to 4500 seconds (Appendix A) shows that the temperatures in the two upper middle locations become nearly the same. The convergence is attributed to "heat soaking" of the entire particle bed.

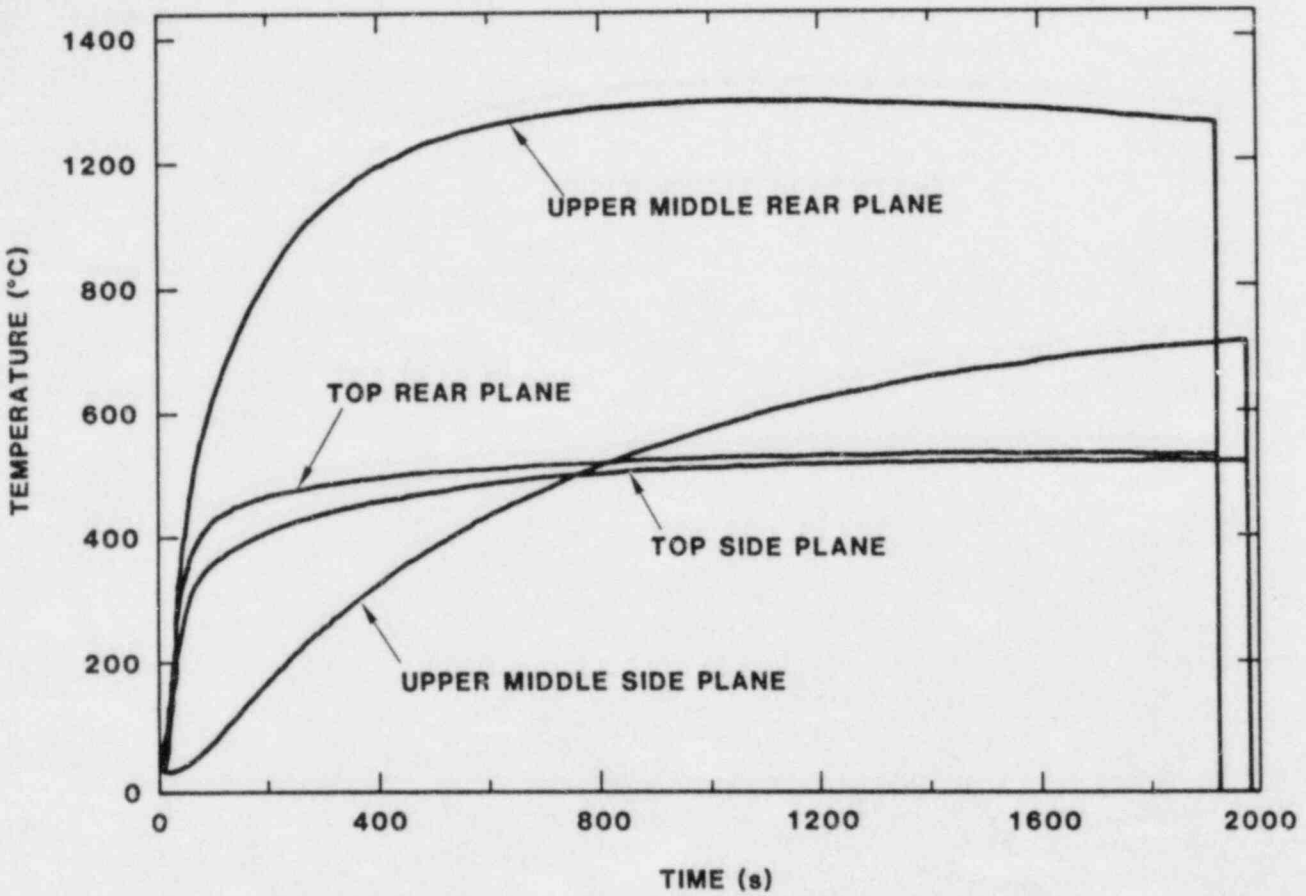


Figure 31. Temperature Histories for Top and Upper Middle Crucible Sidewall Thermocouples

Curves of deposited heat flux as a function of time were obtained for each of the thermocouple locations. The results for the brick thermocouples are not accurate due to the presence of water in the ceramic used to place the devices. The energy required to vaporize the entrained water causes an arrest (plateau) in the temperature profile. Without knowing the quantity of water present, the heat flux method used cannot account for the energy required to induce the phase change.

Total heat flux was obtained by piece-wise integration of each of the heat flux curves. Figure 32 shows the total heat flux values as a function of time for the thermocouple locations that were protected by the particle bed. Data beyond 2600 seconds are not included. The results indicate that the heat flux values for the upper middle side plane and lower middle rear

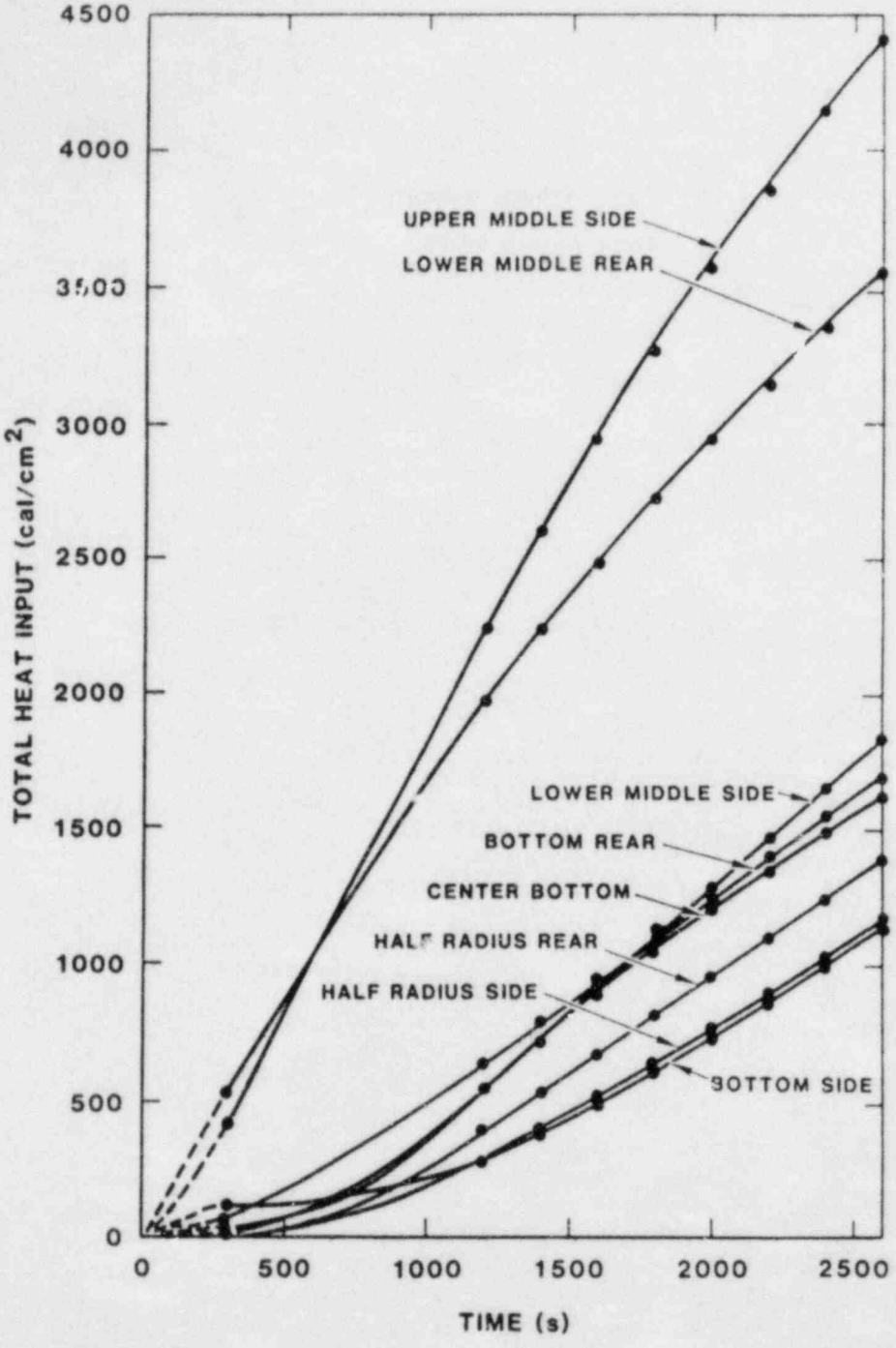


Figure 32.

Total Heat Calculations at the Surface Adjacent to Thermocouple Locations

plane are predominantly higher than the data from all other sensors. The former two sensors reside in areas with the least amount of particle bed protection. The total heat flux values at later times have nominally the same slope, i.e., 0.63 cal/cm$^2$-sec, indicating that an equilibrium condition has been achieved.

Figure 33 shows the correlation between maximum inferred heat flux as a function of the distance of the measuring location from the melt. In all cases, the distance represents the shortest path-length from the crucible wall to the melt front. The coherent iron oxide layer thickness is included in the distance measurement. Unfortunately, the limited size of the apparatus prevented extensive variation in the extent of bed protection. The bed depth range is from 1.5 to 6.0 cm. The data from the three unprotected thermocouple locations are not included in the figure.

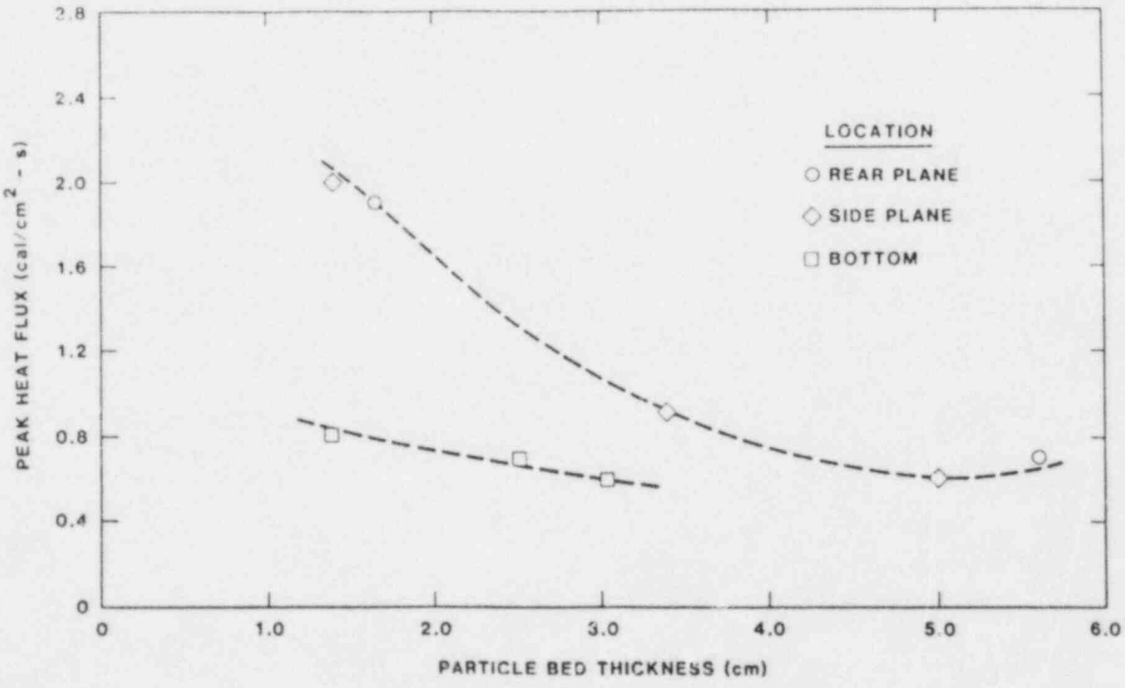


Figure 33. Correlation of Peak Heat Flux vs. Thickness of Particle Bed at Measurement Location

The results shown in Figure 33 suggest that the radial and downward heat fluxes are not the same for bed thicknesses of less than 3.0 cm. The lower values seen in the downward direction are attributed to the greater amount of bed material surrounding the bottom thermocouples. The curvature of the crucible prevents an equivalent amount of material at the sidewall locations. The trend in the data implies that the heat fluxes/values are converging for beds greater than 3.0 cm, as would be expected from conduction heat transfer considerations.

The peak heat flux values are roughly an order-of-magnitude lower than those calculated for a thermocouple protected only by 1 cm of crucible wall. Heat flux values of 2 cal/cm$^2$-sec or more can cause decomposition and melting of most reactor concretes (Ref. 8). Additional analytical and experimental work needs to be performed to determine if bed thicknesses typical of reactor installations are adequate to protect the concrete structure.

In a reactor accident, the thermal energy of the core will eventually be deposited into the particle bed. As the particle bed tests have shown, the bed temperature continues to increase with time. The net effect of the bed is to reduce and delay the peak heat flux values. However, a portion of the thermal energy can be removed if a technique for actively cooling the bed is available.

The heat fluxes calculated for these tests are sufficient to initiate water boiling at atmospheric pressure conditions (Ref 9). Cooling water, introduced into the bed from beneath the melt, would boil and rise through the bed. Additional thermal energy would be absorbed as the vapor comes in contact with the melt. The natural porosity of the bed would lend itself to even distribution of the coolant flow. The total heat content removed may be sufficient to minimize damage to the concrete structure.

## F. Thermal Conductivity Correlations

Particle beds similar to the one used in the experiment have a much smaller effective thermal conductivity than that of the solid phase alone. In the model proposed by Imura and Takegoshi (Ref 10), the ratio of the effective conductivity to the gas conductivity is given as a function of bed porosity, and the ratio of solid-to-gas conductivity. Substituting conductivity values and using an estimated porosity of 0.41 yields an effective thermal conductivity of $1.1 \times 10^{-3}$ cal/cm-s-C, which is more than an order of magnitude less than for the solid phase alone.

A second, slightly more complicated model, is attributed to Luikov, et al. (Ref 11). Their equation contains several empirical coefficients which must be evaluated for the particular system of interest. Using typical values for the various parameters in the iron oxide particle bed used in the experiment gives an effective conductivity of $1.6 \times 10^{-3}$ cal/cm-s-C. The difference between this result and the result obtained from the previous correlation is not significant and within the variation in parameters. In high-temperature applications, the effective thermal conductivity should be augmented by an additional term which accounts for radiative heat transfer across the gas gap between particles. The two models which bracket the magnitude of this effect are the Luikov cell model (Ref 11) and the Vortmeyer pseudo-homogeneous model (Ref 12).

The correlations indicated above for the iron oxide particle bed yield effective thermal conductivities significantly less than the solid phase. Quantitatively, the reductions appear to be nearly an order-of-magnitude at similar temperatures. The form of the correlations suggests that equivalent factors of reduction can be obtained for beds of other metallic oxides, including high-refractories.

## V. Summary

The tests described in this report were designed to evaluate specific aspects of the particle-bed core retention concept. The experiments simulate an accident sequence wherein the reactor vessel is at low or ambient pressure when the failure of the vessel occurs. An iron oxide/aluminum thermite was employed to yield a molten mixture of iron and alumina. The particles were linearly scaled from the sizes conceived for reactor installations.

The test results show that the hydraulic forces exerted by the melt stream do not grossly displace the particle bed. Upon contact, freezing of the melt prevents penetration into the bed beyond a few millimeters. Conduction and convective circulation in the melt causes subsequent heating of the frozen region and heat transfer into the bed. The elevated temperature of the bed allows most of the penetration, over 5 cm, to occur in a time span of less than 5 seconds. This period is then followed by a more gradual movement over the next 45 seconds. The maximum total penetration was approximately 7 cm.

The penetration is caused by melting of the iron oxide particles in contact with the melt. The molten iron oxide combines with both the metallic and oxidic portions of the melt to give mass increases averaging 9% in the iron phase, and 64% to 74% in the alumina. The weight gain corresponds closely with the amount of iron oxide displaced from the original bed configuration. A nominally 1-cm-thick layer of melted and sintered iron oxide material was found in all areas where the melt was in contact with the bed. The microstructure of this region suggests that the cooling of the layer occurred quickly relative to the iron phase. The freezing of this layer appears to be responsible for halting the penetration. The layer is comprised of melted and sintered particles with the extent of sintering corresponding to the distance from the melt boundary.

Material recovered from the iron-oxide-bed residue showed very little (<5% of total mass) fragmentation of the particles. Approximately 7.8% of the material was larger in size, principally because of sintering of individual particles. It is not apparent that more shock-resistant materials are needed to prevent thermal shock of the particles.

Photomicroscopic inspections of various areas of the solidified iron phase indicates the cooling of the material was slow and continuous. The large grain size structure is consistent throughout the specimen studied with the calculated grain index number similar to that seen for an air- or oven-cooled steel melts. Voids within the structure suggest that solidification occurred first at the outer boundaries in contact with the

iron oxide bed and then propagated inward. The relatively slow cooling pattern is attributed to the insulating effect provided by the particle bed, crucible wall, and overlying alumina phase layer.

Heat flux data determined from analysis of thermocouple records placed in the crucible wall indicate that the particle bed was effective in reducing the peak heat flux value and delaying in time the maximum flux. Peak flux values within the bed structure were less than the critical value for using water coolant. This behavior suggests that coolant introduced at the bottom of the particle beds may be adequate to insure protection of the underlying concrete structure.

## APPENDIX A

THERMOCOUPLE TEMPERATURE HISTORIES

This section contains the individual temperature histories from the thermocouples embedded in the crucible wall and magnesium oxide brick located above the melt. Figure 5 gives specifics of each thermocouple location.

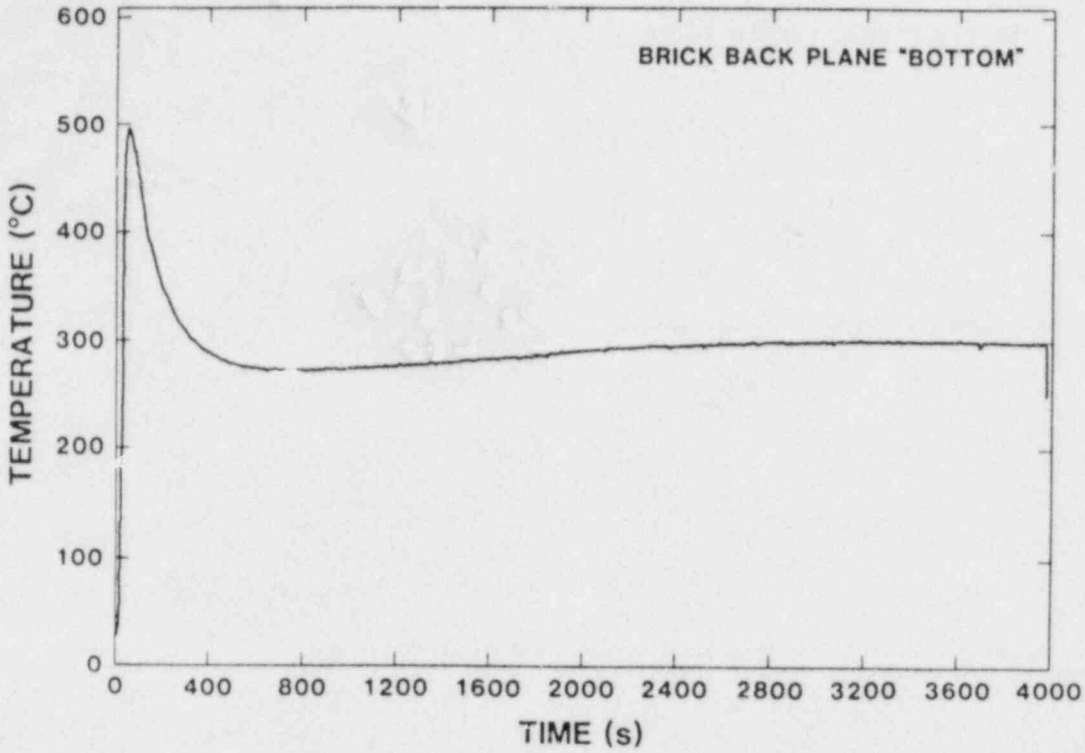


Figure A-1. Brick TC Data PARTICLE BED II

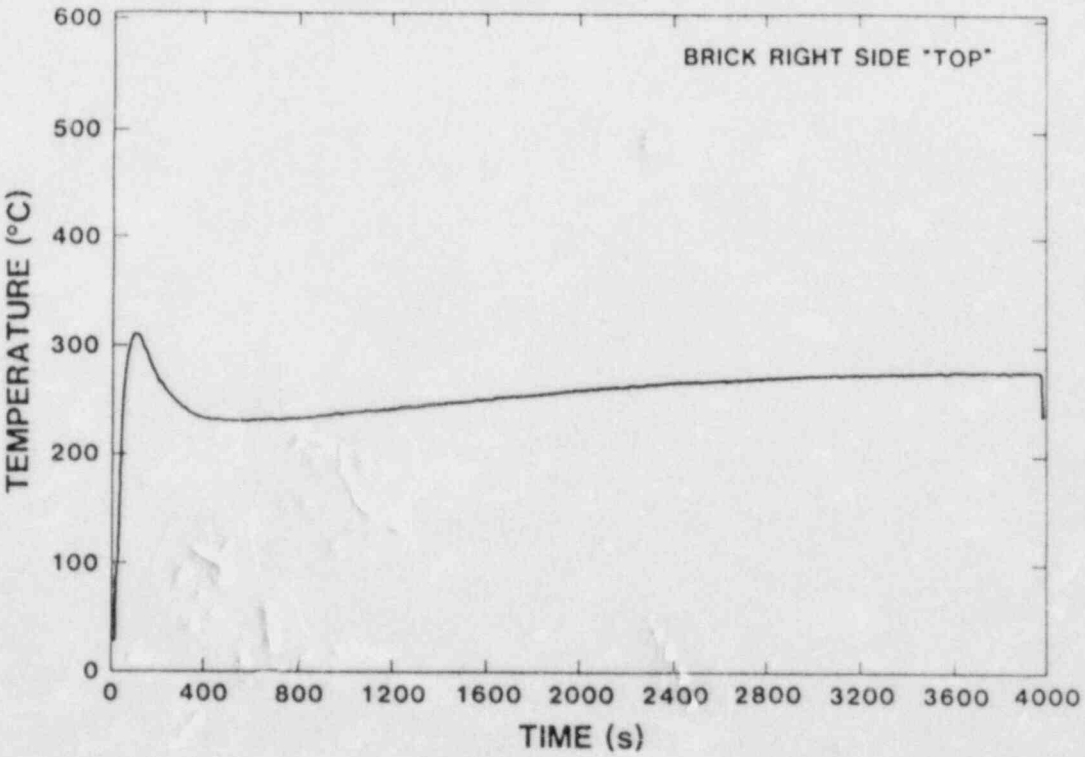


Figure A-2. Brick TC Data PARTICLE BED II

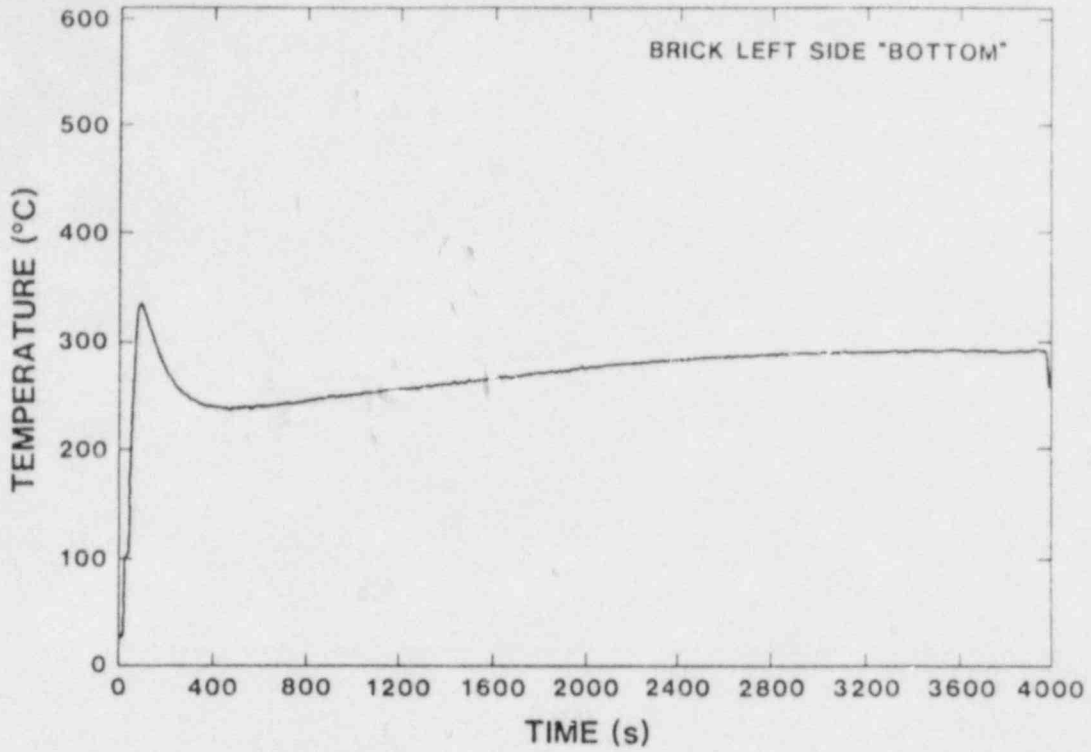


Figure A-3. Brick TC Data PARTICLE BED II

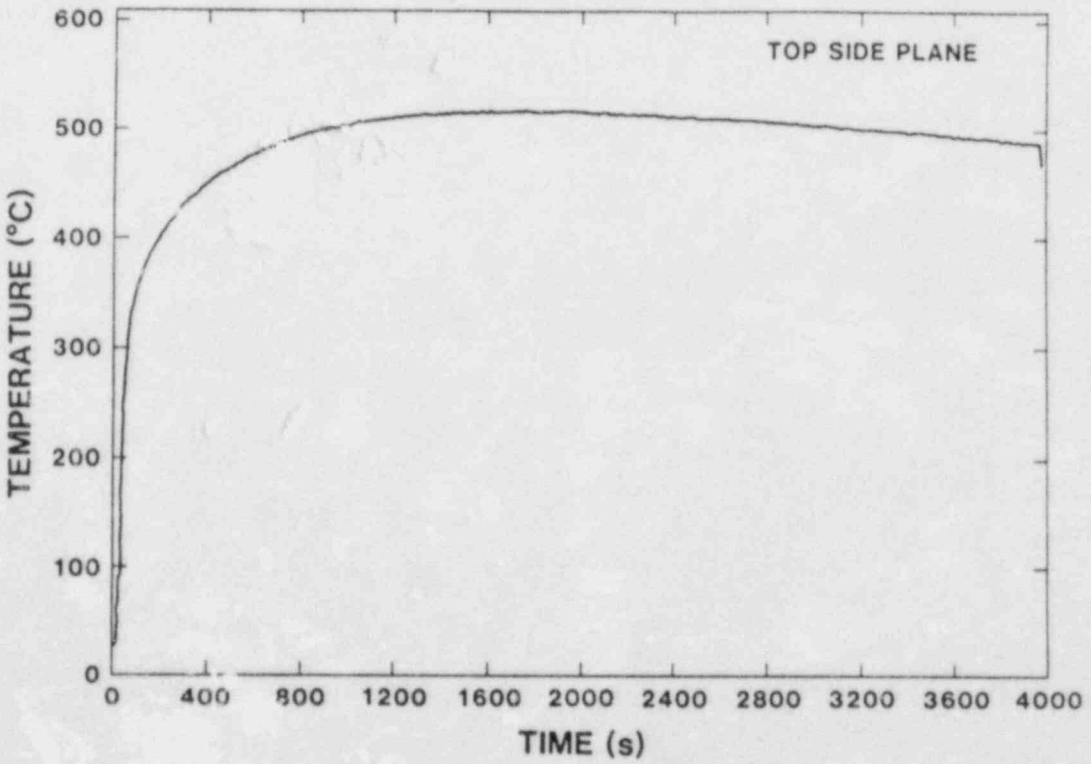


Figure A-4. Crucible TC Data PARTICLE BED II

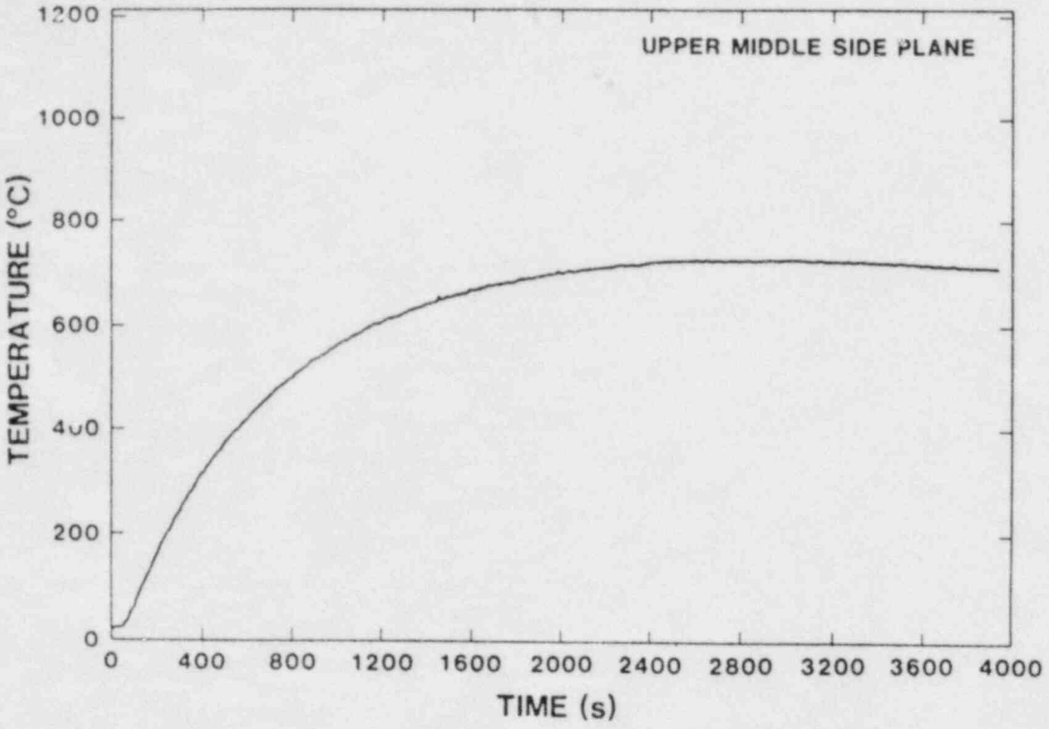


Figure A-5. Crucible TC Data PARTICLE BED II

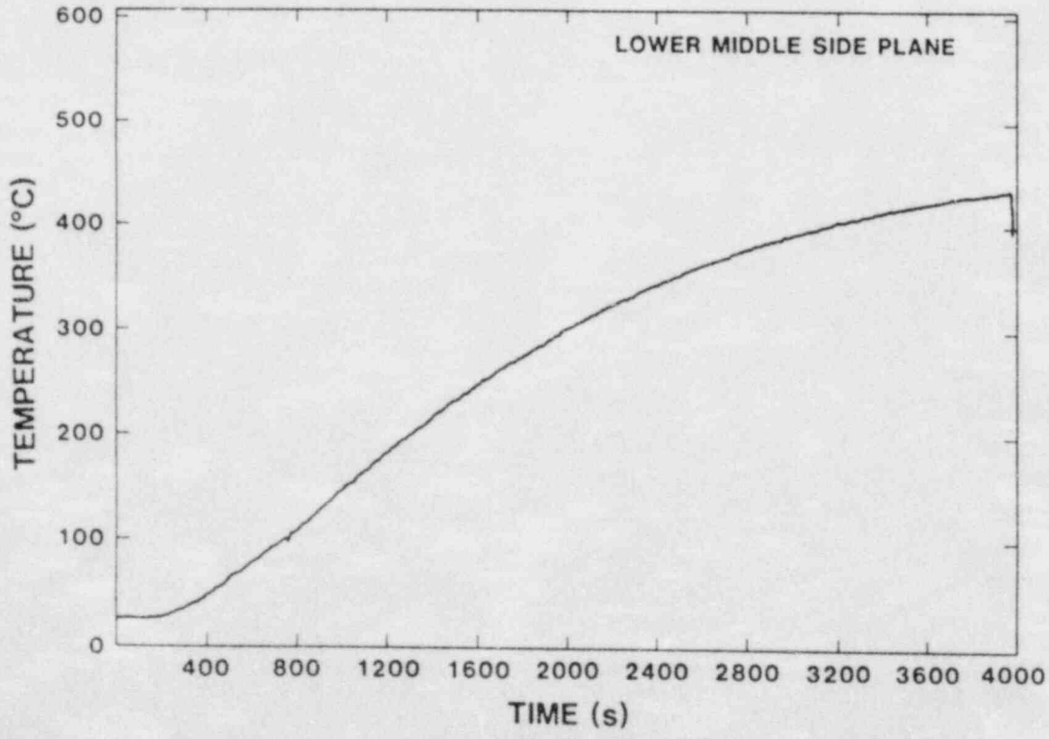


Figure A-6. Crucible TC Data PARTICLE BED II

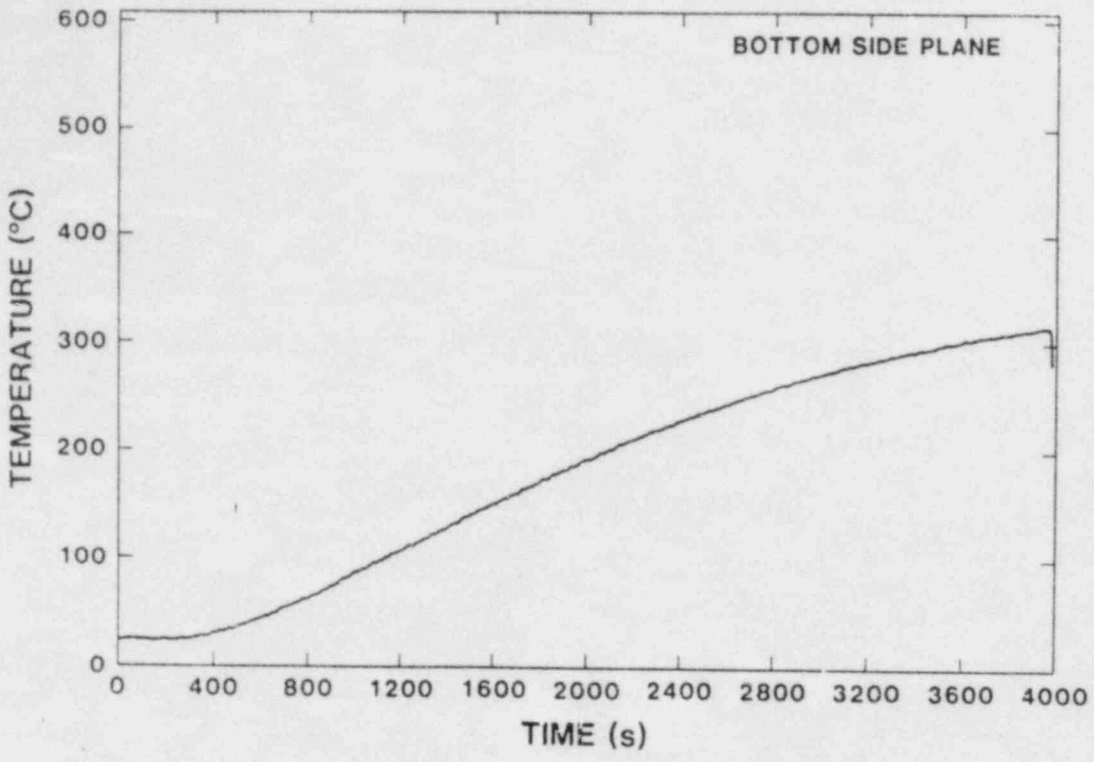


Figure A-7. Crucible TC Data PARTICLE BED II

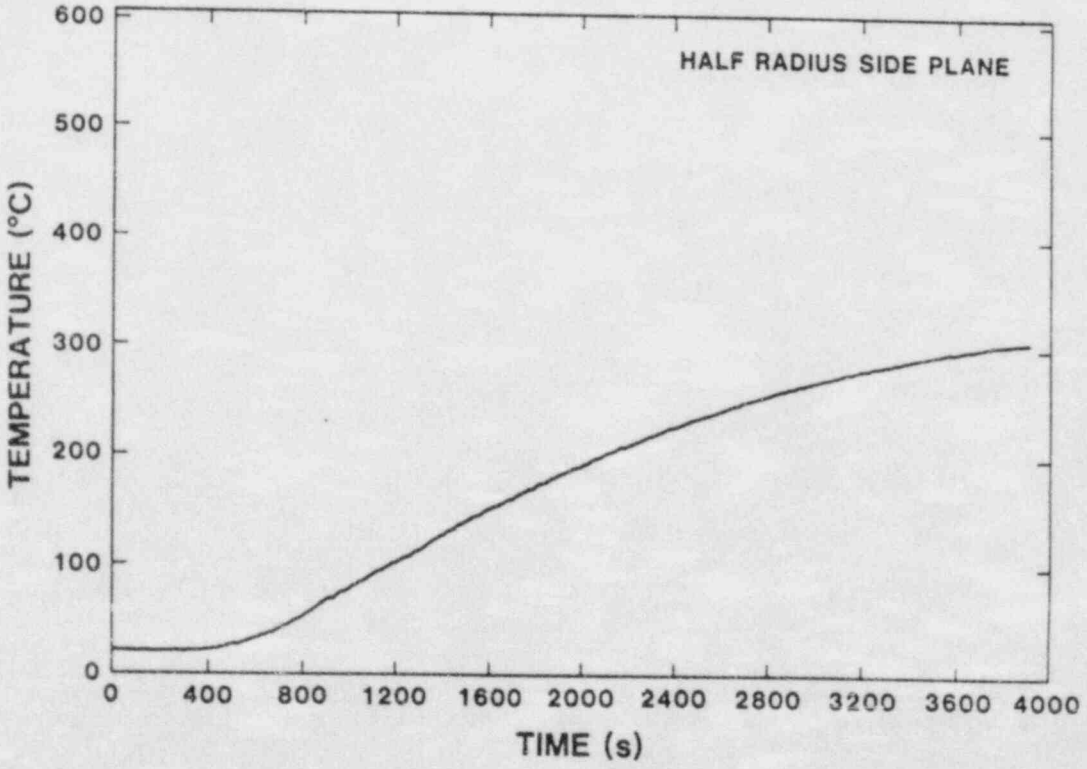


Figure A-8. Crucible TC Data PARTICLE BED II

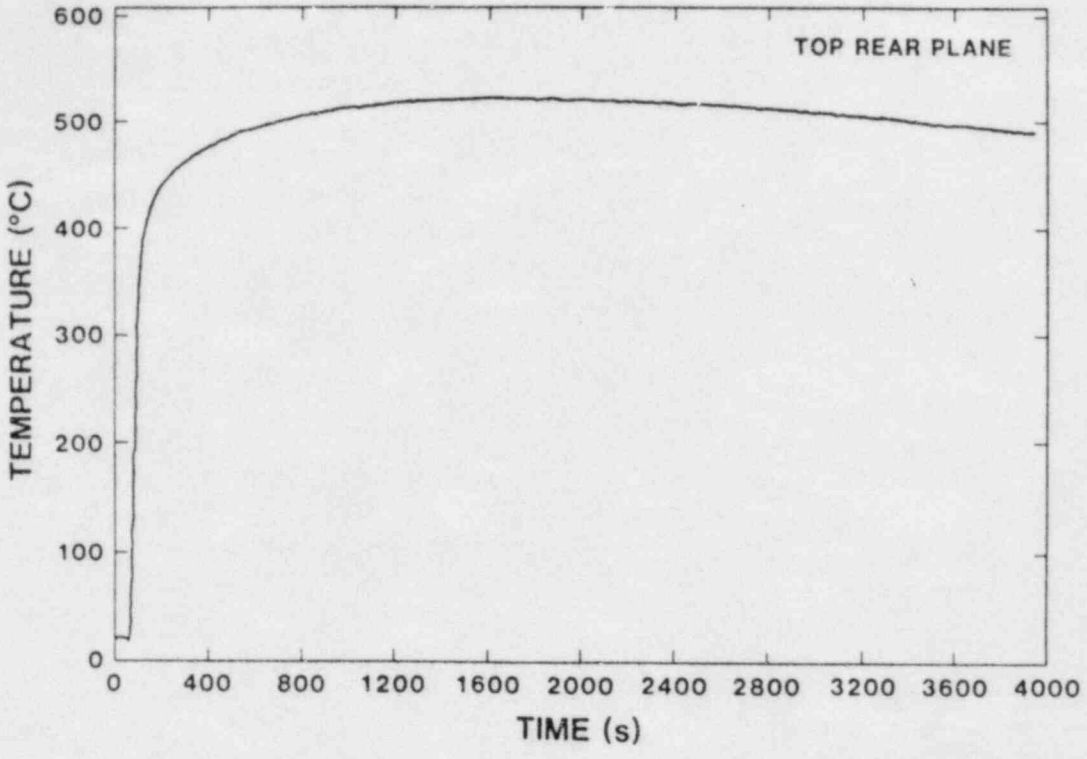


Figure A-9. Crucible TC Data PARTICLE BED II

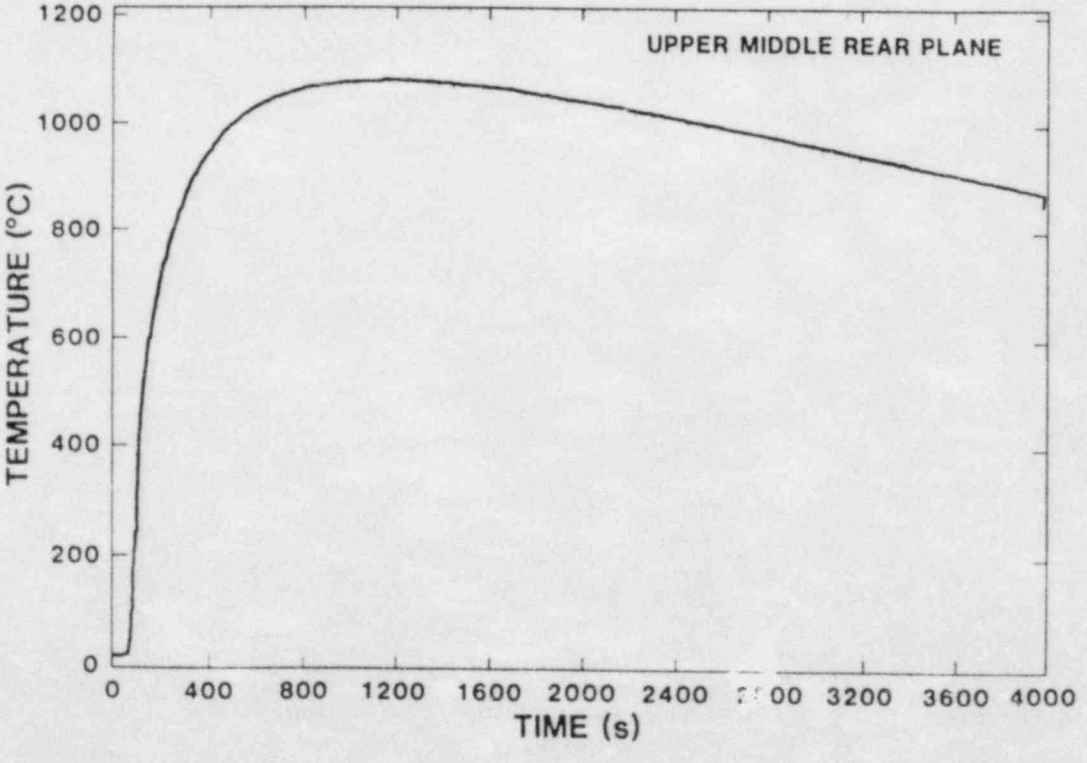


Figure A-10. Crucible TC Data PARTICLE BED II

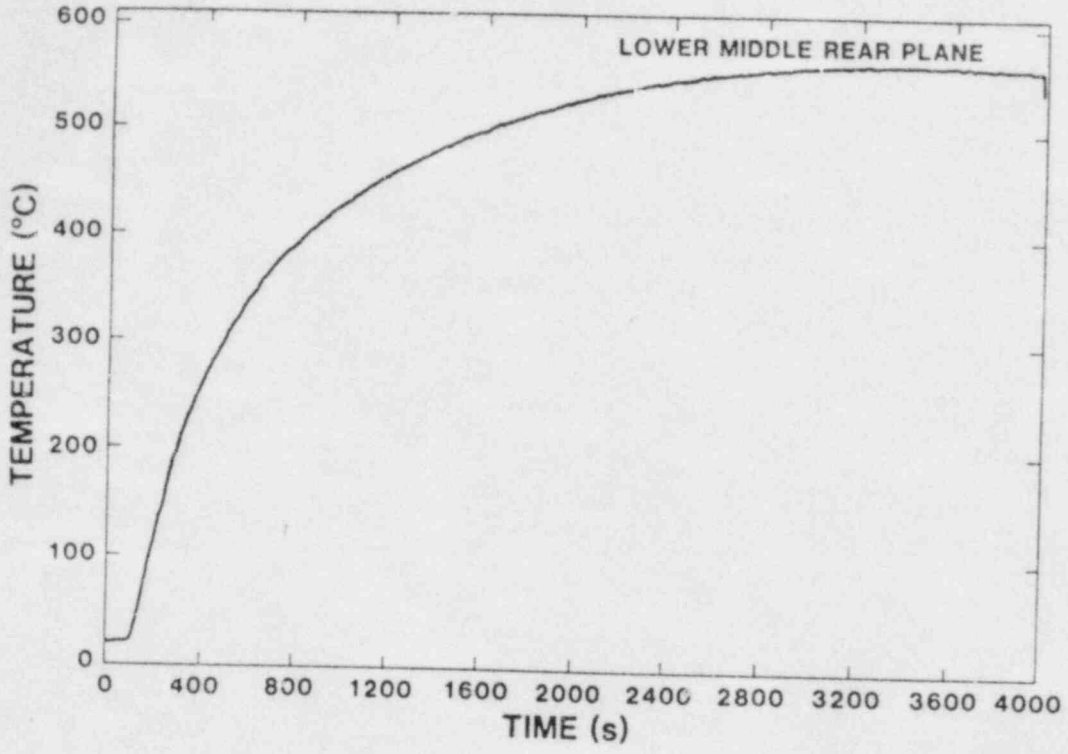


Figure A-11. Crucible TC Data PARTICLE BED II

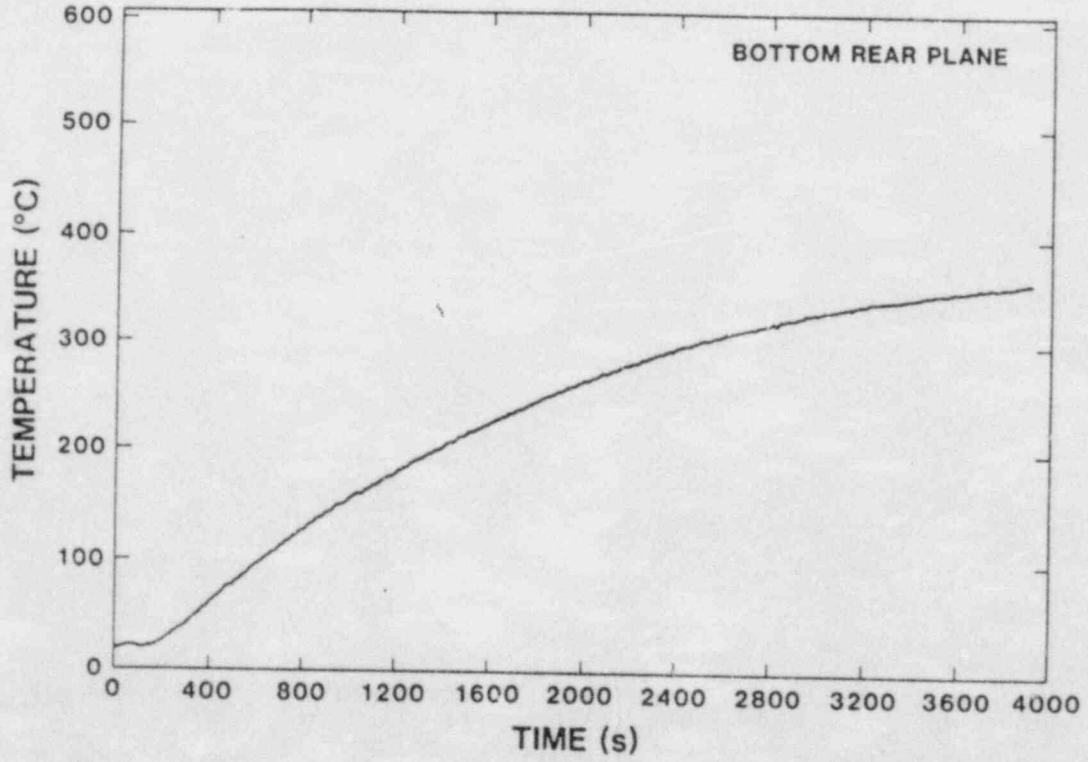


Figure A-12. Crucible TC Data PARTICLE BED II

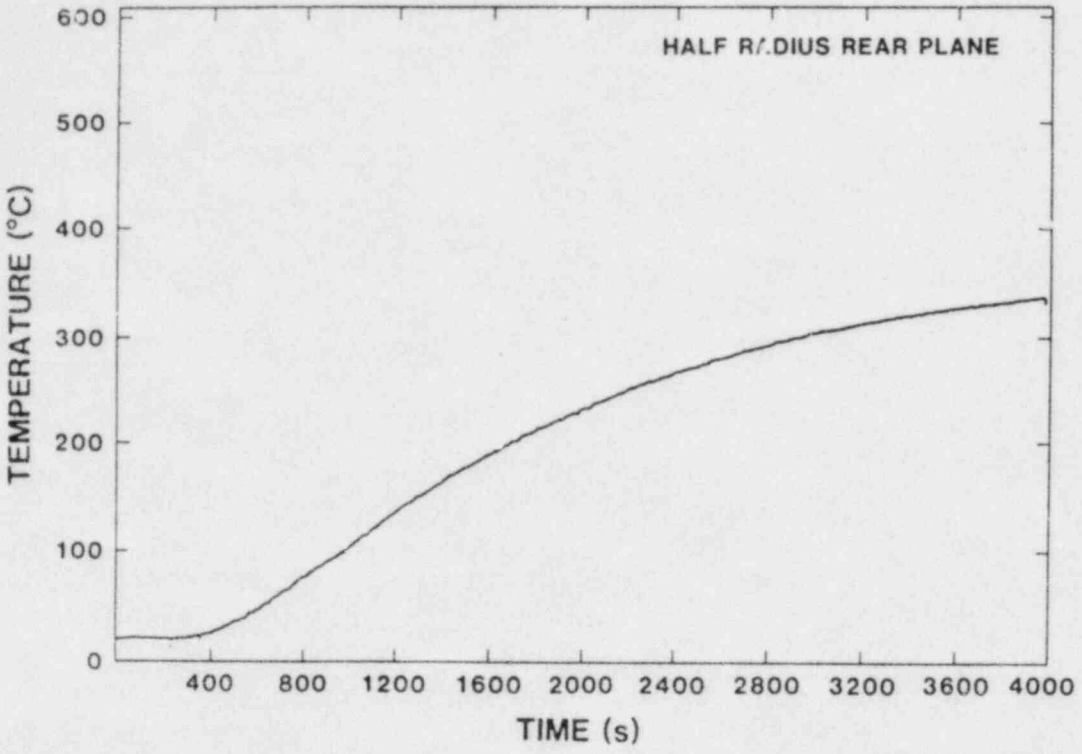


Figure A-13. Crucible TC Data PARTICLE BED II

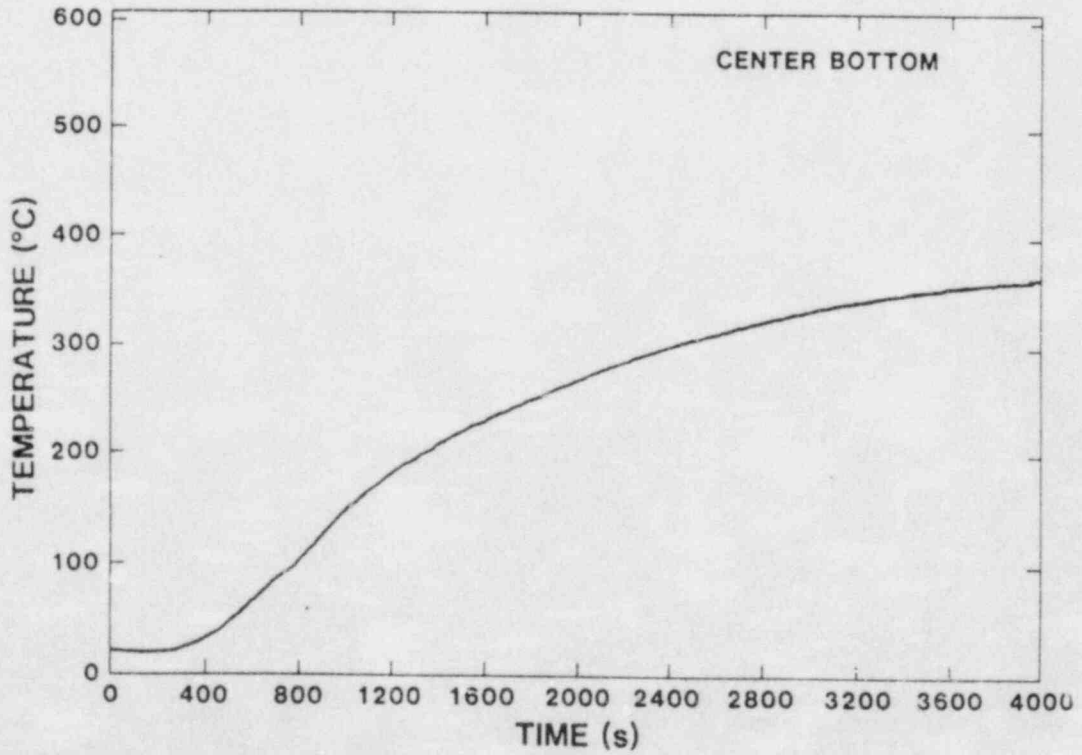


Figure A-14. Crucible TC Data PARTICLE BED II

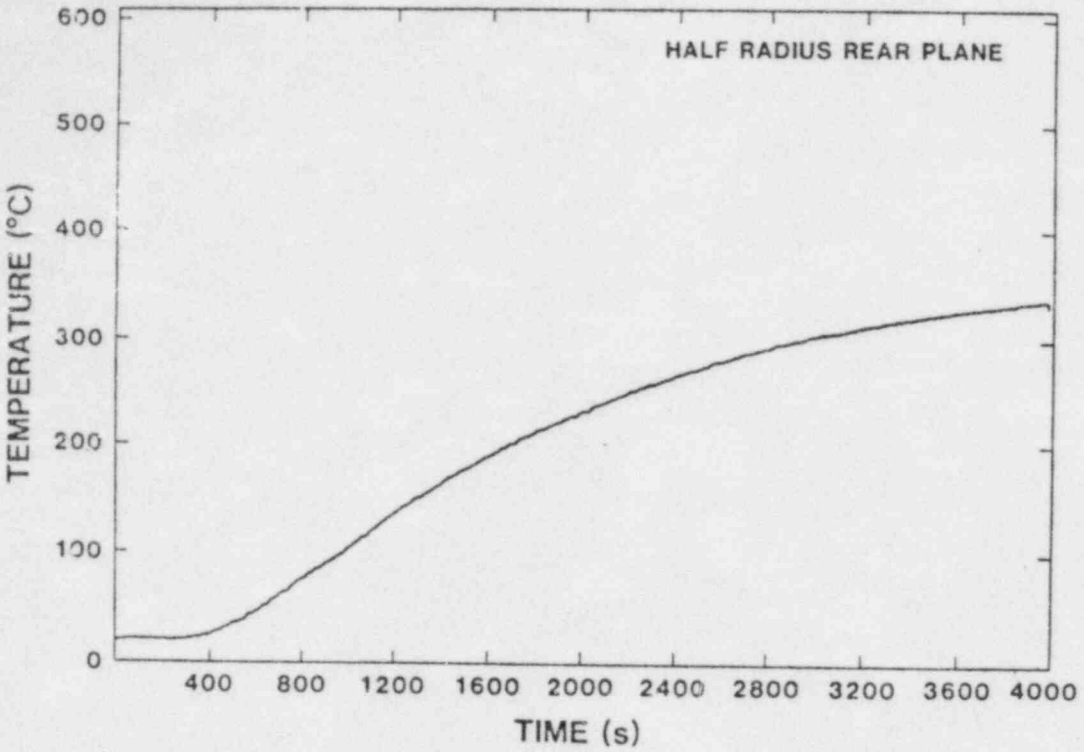


Figure A-13. Crucible TC Data PARTICLE BED II

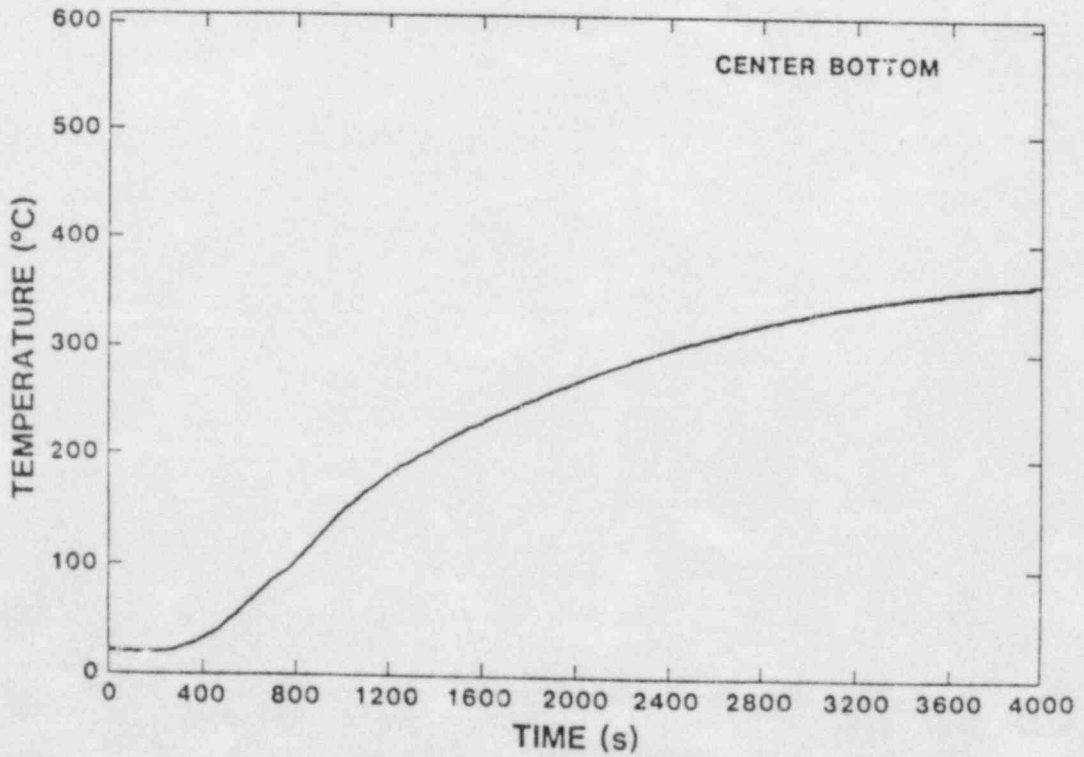


Figure A-14. Crucible TC Data PARTICLE BED II

## APPENDIX B

## HEAT FLUX CALCULATIONS

### A. Estimates of the Heat Flux at the Bed Perimeter

One favorable aspect of a particle bed as a core retention device is its ability to mitigate and delay the peak heat flux to the surrounding concrete structure. Limiting heat fluxes to the concrete reduces the risk associated with the release of aerosols and noncondensable gases and basemat penetration. Heat fluxes to the boundaries of the particle beds used in these experiments were estimated from an inverse heat conduction calculation using the temperature data obtained from thermocouples embedded in the magnesia crucible.

The procedure for deriving the heat fluxes was based on the following assumptions:

(1) The thermocouples are embedded in a semi-infinite, one-dimensional mass with a time-varying surface temperature.

(2) The time variation in the surface temperature is given by

$$T(x = 0, t) - T_o = a_o + \sum_{i=1}^{6} a_i (t)^{i/2}$$

where $a_i$ (i = 0 to 6) are parameters to be determined from the data, $T_o$ is the initial temperature, and T(x, t) is the temperature at position (x) and time (t).

(3) The thermal diffusivity, , and the thermal conductivity, k, of the magnesia are temperature-independent and had the values:

$$= 0.040 \text{ cm}^2/\text{s}$$

(Ref. 9)

$$k = 0.024 \text{ cal/s-cm-}^{o}\text{C}$$

(4) Thermal conduction along the sheath of the thermocouples was negligible.

The first assumption is probably adequate even for thermocouples

embedded in the cylindrical walls and bottom of the magnesia crucible. The radius of curvature of the crucible is large and the thermal conductivity of the magnesia is sufficiently low that no significant error would be expected from this assumption of flat geometry.

The assumed form of the surface temperature is adequate for surfaces not exposed directly to the melt. The estimation procedure outlined below is not satisfactory for situations in which melt contacts and freezes on the surface above a thermocouple because the thermal resistance of the crust affects the magnesia diffusivity assumption.

The assumed temperature independence of the thermal conductivity (and diffusivity) is not correct, but thermal conductivity enters the estimation at a square root. Therefore, the error in the derived heat fluxes ($\delta F$), owing an error in the thermal conductivity ($\delta k$), is given by:

$$\frac{\delta F}{F} = 1/2 \left(\frac{\delta k}{K}\right)$$

Even with the deamplification of errors in the thermal properties, the thermal properties are the biggest source of error in the estimates.

The orientation of the thermocouples and the relatively high thermal conductivity of magnesia relative to stainless steel ($k = 0.034$ cal/s-cm-$^{o}$C) give confidence that the presence of a thermocouple will not introduce serious error in the estimations.

The temperature data were fit to an expression for temperature within a one-dimensional, semi-infinite body with a time-varying temperature:

$$T(x,t) - T_o = a_o \operatorname{erfc} \frac{x}{2\sqrt{\alpha t}} + \sum_{n=1}^{6} a_n \Gamma\tfrac{1}{2}\, n + 1\, (4t)^{\frac{n}{2}}\, i^n \operatorname{erfc}\left[\frac{x}{2\sqrt{\alpha t}}\right]$$

where:

$\Gamma(y)$ = gamma function of y

$$\operatorname{erfc}(y) = \frac{2}{\Pi} \int_{y}^{\infty} \exp\,(-y)^2\, dy$$

$$i^n \text{ erfc}(y) = n^{th} \text{ integral of erfc}(y)$$

The fitting was done by a Marguardt nonlinear, least-squares procedure (Ref. 11) to obtain values of the parameters, $a_i$ for i = 0 to 6. The quality of the fit was assessed by the parameter

$$C = \sum_{i=1}^{n} \left( T(x, t_i) - Y_i \right)^2 / (N - 7)$$

where:

$T(x, t_i)$ = temperature at location x and time $t_i$ calculated from the above equation,

$Y_i$ = temperatureat location x andtime $t_i$ measured in the experiment,

N = the number of temperature observations.

The probable error in the fit is $2/3(C)^{1/2}$. Values of the probable error for the various data sets are listed in Table B-1.

The temperature distribution within the magnesia was differentiated at x = Ø to obtain the heat flux at the surface of the magnesia:

$$\text{Flux } (x = 0, t_i) = -k \frac{\partial T(x = 0, t_i)}{dx}$$

Values of the maximum heat flux and the time of maximum heat flux are listed in Table B-1.

## B. Qualification of the Procedure for Estimating Heat Fluxes from Temperature Data

To demonstrate that the inverse heat conduction method for estimating heat fluxes is suitable, the procedure was also applied to data calculated for a body exposed to a sinusoidal heat flux. The assumed form of the heat flux to the surface of a semi-infinite solid with thermal diffusivity and thermal conductivity k is:

$$\text{Flux } (x = Ø, t) = F_o \sin (\omega t)$$

where:

$F_o$ = 7 cal/cm$^2$-s,

t = time (0 to 4000 secs),

TABLE B-1

Values and Time of Maximum Heat Flux

| Name of Data Set | Location of Thermocouple Below the Heated Surface (cm) | Probable Error in the Fit of Temperature Data ($^{o}C$) | Maximum Heat Flux ($cal/cm^2$-s) | Time of Maximum Heat Flux (s) |
|---|---|---|---|---|
| Bottom Side Plane | 0.76 | 0.38 | 0.6 | 2460 |
| Lower Middle Side Plane | 0.76 | 0.64 | 0.9 | 1943 |
| Upper Middle Side Plane | 0.76 | 1.08 | 2.0 | 491 |
| Top Side Plane | 0.76 | 2.36 | 7.9 | 19 |
| Bottom Rear Plane | 0.76 | 0.35 | 0.7 | 1763 |
| Lower Middle Rear Plane | 0.76 | 0.65 | 1.9 | 204 |
| Upper Middle Rear Plane | 0.76 | 2.92 | 16.1 | 18 |
| Top Rear Plane | 0.76 | 3.14 | 9.2 | 26 |
| Center Bottom | 0.49 | 1.06 | 0.8 | 1346 |
| Half-Radius Side Plane | 0.49 | 0.44 | 0.6 | 2312 |
| Half-Radius Rear Plane | 0.49 | 0.50 | 0.7 | 1839 |

$\omega$ = 180/4000 degrees of arc.

The sinusoidal form of the heat flux is not immediately represented in terms of a polynomial, as assumed in the estimating procedure. Thus, the data calculated with this heat flux should be a good test of the method. Restricting the test to one-half cycle of the heat flux, data similar in temporal variation to that obtained in the particle bed test should be obtained.

The temperature at a distance x from the surface exposed to the sinusoidal heat flux is given by:

$$T(x, t) - T_o = \frac{\sqrt{\alpha}}{k\sqrt{\pi}} \int_0^t \frac{F_o \sin(\omega t - y) \exp(-x^2/4\alpha y)\, dy}{\sqrt{y}}$$

$$= \frac{F_o\sqrt{\alpha}}{k\sqrt{\pi}} \left[ \sin(\omega t) \int_0^t \frac{\cos(\omega v) \exp(-x^2/4\alpha y)\, dy}{\sqrt{y}} \right.$$

$$\left. - \cos(\omega t) \int_0^t \frac{\sin(\omega y) \exp(-x^2/4\alpha y)\, dy}{\sqrt{y}} \right]$$

where $T_o$ is the temperature at the point x at zero time. The above integral expression is evaluated at 100 points evenly distributed over the closed interval of 1 to 4000 s. No special care in the programming is taken to account for computational pathology in evaluating the integral expression near zero time. Consequently, the temperatures at early times are expected to be inaccurate.

In general, the estimation procedure yields excellent results for times between 200 and 3500 seconds (i.e., heat flux values of 1 to 7). The disagreement between the assumed and estimated heat fluxes is greatest for very early times. This disagreement is expected and is probably the result of numerical inaccuracies in the calculated data and the difficulty of differentiating the spatial temperature distribution for very small temperatures.

Disagreement between estimated and assumed heat fluxes at late times is also observed. This disagreement arises because no data exist on temperatures within the solid to demonstrate the

effects of changes in the heat flux at the surface at late times. Errors in the estimated heat flux at late times become more pronounced as the distance between the surface exposed to the heat flux and the point at which temperature data are collected increases.

The standard error in the fit of the temperatures within the solid exposed to the sinusoidal heat flux indicates a probable error of about 1.2°C. The linear correlation of the assumed and estimated heat flux has a slope of 1.00696 ±0.00340 and an intercept of -0.03787 ±0.01692. Ideal correlation would yield a slope of 1 and an intercept of zero. The deviation of the actual and ideal correlation is due primarily to the errors in the first few estimated heat fluxes.

Integration of the heat flux data yields the heat input to the surface adjacent to the point where temperature data are collected. The correlation of assumed and estimated heat inputs has a slope of 0.999958 $\pm 8.5 \times 10^{-5}$ and an intercept of 48.98 ±0.94. This indicates that the error in the first few data points (those near the intercept) is nearly totally responsible for the error in the correlation. If the first estimated point is corrected and the correction of this point carried through the integral, the slope of the correlation is unaffected, but the intercept is reduced to 2.75 ± 0.35.

The procedure was also tested in the following two ways:

(1) Data calculated as above were made "noisy" by adding random numbers between -5 and +5 to the calculated temperatures.

(2) Data calculated as above were "smoothed by a simple procedure defined by:

$$T^{(i)}_{Smooth} = \frac{1}{6}\left( 4T^{(i)} + T^{(i+1)} + T^{(i-1)} \right)$$

Parameters characterizing the estimated are collected in Table B-2. The two data treatments, ± 5°C noise and smoothing, degraded the agreement between assemed and estimated heat fluxes. "Noise" in the data has a larger effect than smoothing. The degradation was not serious in either case. The estimation procedure appears to be insensitive to these treatments of the data.

A final test of the estimation procedure is created because of the experimental difficulty in accurately locating a temperature sensor at a point in a solid. Temperature data are calculated as described above for a point 0.702 cm below the surface exposed to a sinusoidal heat flux. The estimation procedure is then applied to these temperature data assuming that the data are

for a point 0.762 cm below the heated surface.

Errors in thermocouple location produce greater errors in the estimated surface heat flux than either of the data modifications described above. Although the errors in surface heat flux are the largest experienced, the extent of the error is not great and appears insensitive to errors in thermocouple location. This result adds confidence to results obtained from the particle bed test data.

TABLE B-2

Parametric Values Obtained for Qualification of the Estimation Procedure

| Parameter | Calculated Data | Test Technique | | |
|---|---|---|---|---|
| | | Noisy Data | Smoothed Data | Improper Location |
| Probable Error in Temperature Fit | 1.187 | 1.784 | 1.192 | 1.191 |
| Maximum Heat Flux | 6.99967 | 7.00479 | 6.99830 | 7.03657 |
| Time of Maximum Heat Flux | 1988.62 | 1987.790 | 1988.60 | 1981.67 |
| Slope of Linear Correlation of Assumed and Estimated Heat Fluxes | 1.00696 ±0.00388 | 1.00733 ±0.00352 | 1.00657 ±0.00334 | 1.01391 ±0.00365 |
| Intercept of Linear Correlation of Assumed and Estimated Heat Fluxes | -0.03878 ±0.01692 | -0.03994 ±0.01752 | -0.03769 ±0.01662 | -0.0505 +0.01815 |

## REFERENCES


1. D.A. Powers and F.E. Arellano, Large-Scale, Transient Tests of the Interaction of Molten Steel with Concrete, SAND81-1753, NUREG/CR-2282 (Albuquerque, NM: Sandia National Laboratories, January 1982.

2. D. Perinic, et al., Concrete Crucible with Thermite Melts, (Translation on NRC 669), Kfk 2572 (Karlsruhe, FRG: Nuclear Research Center, Karlsruhe, Inc.).

3. G.D. Fish, M. Pilch, and F.E. Arellano, "Particle-Bed Core Retention Concept: Preliminary Assessment", SAND82-2545, NUREG/CR-3042, March 1983.

4. D.A. Powers and F.E. Arellano, Direct Observation of Melt Behavior During High Temperature Melt/Concrete Interactions, SAND81-1754, NUREG/CR-2283 (Albuquerque, NM: Sandia National Laboratories, January 1982).

5. C.R. Barrett, et al., The Principles of Engineering Materials, Prentice-Hall, Inc., (Edgewood Cliffs, NJ: 1973).

6. 1978 Annual Book of ASTM Standards, PART II, (Philadelphia, PA: American Society for Testing and Materials).

7. Metals Reference Book, 5th Ed., 1926, C.J. Smithells (Ed.) (Woburn, MS: Butterworths Publishing, Inc.)

8. J.F. Muir, Response of Concrete Exposed to a High Heat Flux on One Surface, SAND77-1467 (Albuquerque, NM: Sandia National Laboratories, November 1977).

9. F. Kreith, Principles of Heat Transfer, 2nd Ed. (Scranton, PA: International Textbook Co., 1966).

10. S. Imura and E. Takegoshi, "Effect of Gas Pressure on the Effective Thermal Conductivity of Packed Beds", Heat Transfer Japanese Research, Vol. 4, p. 13, 1974.

11. A.V. Luikov, A.G. Shashkov, L.L. Vsailiev, and Yu. F. Praiman, "Thermal Conductivity of Porous Systems", Int. J. Heat Mass Transfer, Vol. 11, p. 117, 1968.

12. D. Vortmeyer, "Radiation in Packed Solids," 6th Int. Heat Trans. Conf., Toronto, 1978.

13. M. Pilch and P.K. Mast, "PLUGM: A Coupled Thermal-Hydraulic Computer Model for Freezing Melt Flow in a Channel," SAND82-1580 (Albuquerque, NM: Sandia National Laboratories, 1982).

## REFERENCES (CONT.)

14. Data Sheet - NM-MC-6, Norton Industrial Ceramics Division, Norton Co., Wocester, MS, 01606.

15. P.R. Bevington, Data Reduction and Error Analysis for the Physical Sciences, (New York, NY: McGraw-Hill Book Co., 1969).

**DISTRIBUTION:**

U.S. NRC Distribution Contractor (CDSI)
7300 Pearl Street
Bethesda, MD 20014
250 copies for R7

U.S. Nuclear Regulatory Commission (11)
Office of Nuclear Regulatory Research
Washington, DC 20555
Attn: O.E. Bassett
S.B. Burson
R.T. Curtis
C.N. Kelber
M. Silberberg
T. Walker
J. Larkins
M. Jankowski
L. Chan
G. Marino
R.W. Wright

U.S. Nuclear Regulatory Commission (11)
Office of Nuclear Reactor Regulation
Washington, DC 20555
Attn: N. Anderson
V. Benaroya
R.T. Butler
N. Lauben
J.K. Long
J.F. Meyer
A.R. Marchese
A.W. Serkiz
T.P. Speis
Z. Rosztoczy
C.G. Tinkler

U.S. Department of Energy (2)
Albuquerque Operations Office
P.O. Box 5400
Albuquerque, NM 87185
Attn: J.R. Roeder
D.K. Nowlin
For: C.B. Quinn
D. Plymale

U.S. Department of Energy
Office of Nuclear Safety Coordination
Washington, DC 20545
Attn: R.W. Barber

Cathy Anderson
Nuclear Safety Oversight Commission
1133 15th Street NW
Room 307
Washington, DC 20005

Electric Power Research Institute (2)
3412 Hillview Avenue
Palo Alto, CA 94303
Attn: G. Thomas
R. Vogel
D. Squarer

**DISTRIBUTION (CONT.)**

Brookhaven National Laboratories (3)
Department of Nuclear Energy
Building 820
Upton, NY 11973
Attn: T. Pratt
T. Ginsberg
G. Green

I. Catton
University of California, Los Angeles
2567 Boelter Hall
405 Hilgaarde Avenue
Los Angeles, CA 90024

University of Wisconsin (2)
Dept. of Nuclear Engineering
1500 Johnson Drive
Madison, Wisconsin 53706
Attn: M. Corradini
S. Abdul-Kalik

D. Swanson
Applied Sciences Assoc., Inc
P.O. Box 2687
Palos Verdes Peninsula, CA 90274

Argonne National Laboratory (2)
9700 S. Cass Avenue
Argonne, IL 60439
Attn: D. Pedersen
L. Baker

W. Tarbell
Ktech Corporation
901 Pennsylvania NE
Albuquerque, NM 87110

M.L. Stevenson
Los Alamos National Laboratory
P.O. Box 1663
Los Alamos, NM 87545

Professor R. Seale
Dept. of Nuclear Engineering
University of Arizona
Tucson, AZ 85721

**DISTRIBUTION (CONT.)**

R. Tosetti
Bechtel Power Corporation
P.O. Box 3965
San Francisco, CA 94119

K.S. Norwood
Oak Ridge National Laboratory
Building 4500N
P.O. Box X
Oak Ridge, TN 37830

T. Kress
Oak Ridge National Laboratory
P.O. Box Y
Oak Ridge, TN 37830

M. Fontana, Director
IDCOR Program
Technology for Energy, Inc.
P.O. Box 22996
10770 Dutchtown Road
Knoxville, TN 37922

Offshore Power System
8000 Arlington Expressway
Box 8000
Jacksonville, FL 32211
Attn: D.H. Walker

F. Bevilacgua, Vice-President
ombustion Engineering, Inc.
Department 9481-422
1000 Prospect Hill Street
Winsor, CN 06095

Battelle Columbus Laboratory (3)
505 King Avenue
Columbus, OH 43201
Attn: P. Cybulskis
R. Denning
J. Gieseke

Kraftwerk Union (2)
Hammerbacher Strasse 12 14
Postfach 3220
D-8250 Erlangen 2
FEDERAL REPUBLIC OF GERMANY
Attn: M. Peehs
K. Hassman

**DISTRIBUTION (CONT.)**

Project Schneller Brueter
Kernsforschungszentrum KarlsruheGMBH
Postfach 3640
D-75 Karlsruhe
FEDERAL REPUBLIC OF GERMANY
Attn: Dr. Heusener

Gesellschaft fur Reaktorsicherheit (2)
(GRS mbH)
8046 Garching
FEDERAL REPUBLIC OF GERMANY
Attn: E.F. Hicken
H.L. Jahn

Dr. M.V. Banaschik
Gessellschaft fur Reaktorischerheit
(GRS mbH)
Postfach 101650
Glockengasse 2
5000 Koeln 1
FEDERAL REPUBLIC OF GERMANY

Professor F. Mayinger
Techische Universitat Hannover
3000 Hannover 1
FEDERAL REPUBLIC OF GERMANY

AEC, Ltd.
Whiteshell Nuclear Research Establishment
Pinawa, Manitoba
CANADA
Attn: D. Torgerson

Dr. Watanabe
Power Reactor Nuclear Fuel
Development Corporation (PNL)
Fast Breeder Reactor Development
Project FBR
9-13, 1-Chome, Alaska
Minato-Ku, Tokyo
JAPAN

UKAEA (2)
AERE Haswell
Oxon OX11 ORA
ENGLAND, UK
Attn: Dr. L. Gittus, AETB and
Dr. T.R. Matthews, TP Div.

**DISTRIBUTION (CONT.)**

UKAEA (2)
Culham Laboratory
Abingdon
Oxon OX14 3DB
ENGLAND, UK
Attn: Dr. F. Briscoe and
Dr. B.D. Turland

Dr. R.J. Stubbs
HMNII, HSE
Thames House North
Millbank
London SW1P 4QJ
ENGLAND, UK

Berkeley Nuclear Laboratory (2)
Berkely GL13 9PB
Gloucestershire
UNITED KINGDOM
Attn: N.E. Buttery and
J.E. Antill

B. Tolley
Director of Research, Science and
Education
CEC
Rue De La Loi 200
1049 Brussels
BELGIUM

Swedish State Power Board
El-Och Vaermeteknik
SWEDEN
Attn: E. Ahlstroem

Project Nucleate Sicherheit (2)
Kernforschungszentrum Karlsruhe
Postfach 3460
75 Karlsruhe
FEDERAL REPUBLIC OF GERMANY
Attn: J.P. Hosemann
S. Hagan

DISTRIBUTION

1830 M.J. Davis
1836 F.J. Zanner
1840 N. Magnani
3141 C.M. Ostrandes
3151 W.L. Garner
6454 G.L. Cano
6427 M. Berman
6427 R.K. Cole, Jr.
6430 N.R. Ortiz
6400 A.W. Snyder
6410 J. Hickman
6414 A.S. Benjamin
6420 J.V. Walker
6422 D.A. Powers
6422 F.E. Arellano (5)
6422 J.E. Brockmann
6422 R.M. Elrick
6422 J.D. Fish
6422 E. Randich
6422 T. Taig
6422 J. Gronager
6422 E. Copus
6422 W.W. Tarbell (4)
6422 R.E. Blose (5)
6423 P.S. Pickard
6425 W.J. Camp
6425 A.J. Wickett
6425 M. Pilch
6425 D. Bradley
6450 J.A. Reuscher
7530 W.E. Caldes
7537 N.R. Keltner
7537 R.U. Acton
7537 T.Y. Chu
8424 M.A. Pound

120555078377 1 IAN1R7
US NRC
ADM-DIV OF TIDC
POLICY & PUB MGT BR-PDR NUREG
W-501
WASHINGTON DC 20555